JℲM PAPERS

Characteristics of geometry-and pressure-induced laminar separation bubbles at an enhanced level of free-stream turbulence

S. Mohamed Aniffa[1], V.S. Caesar[1], V. Dabaria[1] and A.C. Mandal[1],†

[1]Department of Aerospace Engineering, Indian Institute of Technology, Kanpur 208016, India

Responses of a geometry-induced separation bubble (GISB) and a pressure-induced separation bubble (PISB) at enhanced levels of free-stream turbulence (FST) have experimentally been investigated for a comparative study using the particle image velocimetry (PIV) technique. The outlines of separation bubbles based on the dividing streamlines are self-similar for different levels of FST and Reynolds numbers. The spectral analyses of the time-resolved PIV data show that the vortex shedding frequency of a separated shear layer remains unchanged for the GISB cases even with an enhanced level of FST. In contrast, it is different for the PISB cases. We propose a criterion that determines whether the frequency will remain the same even for the cases with FST. Linear stability analyses reveal that the inviscid-inflectional instability dominates the transition process, and the linear stages of transition are not completely bypassed even at an enhanced level of FST. The most amplified frequencies, while scaling with the displacement thickness and the boundary layer edge velocity, collapse in a single curve for all the cases. Furthermore, measurements in the spanwise plane show that the streamwise velocity streak/Klebanof mode at an enhanced level of FST is not a general flow feature for all types of separation bubbles. However, at an enhanced level of FST for the PISB case, the boundary layer streaks are found to distort the two-dimensional vortex structure associated with the Kelvin–Helmholtz instability, eventually leading to a three-dimensional Λ-like structure in the spanwise plane.

Key words: boundary layer separation, shear-flow instability, transition to turbulence

1. Introduction

The laminar–turbulent transition of a separated shear layer is a fundamental problem in fluid dynamics. A flow can separate from the wall and generate a separation bubble

† Email address for correspondence: alakeshm@iitk.ac.in

either due to a large adverse pressure gradient or due to a sharp corner/blunt leading edge/rounded leading edge. A separation bubble generated due to a large adverse pressure gradient is termed a pressure-induced separation bubble (PISB), while a separation bubble generated due to a sharp corner/blunt leading edge/rounded leading edge is termed a geometry-induced separation bubble (GISB) in the literature (e.g. Diwan & Ramesh 2009; Robinet 2013; Yang 2019). However, at a moderate Reynolds number, separation bubbles are characterized by the shear layer separation from the surface followed by the downstream reattachment onto the surface, which is believed to be due to the entrainment of turbulence in the shear layer (e.g. Dovgal, Kozlov & Michalke 1994; Tani 1964).

The separation bubble emerges in many engineering devices, for example, in wind/gas turbine blades and in the wings of unmanned aerial and micro air vehicles. A separated flow on an aerodynamic body can adversely affect its aerodynamic performance. There have been considerable efforts to understand the dynamics of various separated flows. Nonetheless, several points that are not well understood, need further attention. For example, the effect of upstream turbulence on the dynamics of a turbulent separation bubble, which may also develop instabilities leading to coherent structures, is still not answered, and the separated flows often being noise amplifiers, their dynamics may be susceptible to different upstream conditions, the sensitivity of which is not clear (Robinet 2013). Similarly, the effect of upstream turbulence on the dynamics of a laminar separation bubble is not very clear.

Recently, there has been a renewed interest on the effect of free-stream turbulence (FST) on a separation bubble. Some recent studies (Balzer & Fasel 2016; Stevenson, Nolan & Walsh 2016) reported that the Klebanoff mode, as seen in the case of an attached boundary layer at an enhanced level of FST, is also found to exist for some geometry- and pressured-induced bubbles. On the other hand, for a GISB case, there can be a very short distance for the development of an attached boundary layer or no distance at all for the development of a boundary layer before the point of separation (Yang 2019). A question then arises whether the Klebanoff mode can still be a flow feature for all the GISB cases or not. This is yet to be addressed and answered. This can be better addressed if a comparative experimental investigation on the response of a GISB and a PISB at an enhanced level of FST can be carried out.

1.1. *Geometry-induced separation bubble*

Various works on GISBs were carried out in the past focusing on several aspects, such as the reattachment length, low-frequency unsteadiness, vortex shedding and three-dimensional (3-D) flow features in the separated region (e.g. Lane & Loehrke 1980; Ota, Asano & Okawa 1981; Kiya & Sasaki 1983b; Sasaki & Kiya 1991). In their experimental study, Kiya & Sasaki (1983b) investigated the shedding characteristics of a separation bubble at the blunt leading edge of a flat plate and observed that the regular vortex shedding exists along with low-frequency unsteadiness. Such low-frequency oscillations due to large-scale unsteadiness in a separation bubble generated at the blunt leading edge are further reported experimentally and numerically by various authors (e.g. Cherry, Hillier & Latour 1984; Tafti & Vanka 1991; Yang & Voke 2001). Using 3-D numerical simulation, Tafti & Vanka (1991) postulated that the low-frequency unsteadiness is due to the periodic enlargement and shrinkage of the separation bubble, caused by the mass buildup within the bubble and venting of the fluid in the spanwise direction, respectively.

Vortex shedding followed by the 3-D aspects of a separated shear layer has also been studied in various numerical and experimental works (e.g. Sasaki & Kiya 1991; Tafti &

Vanka 1991; Yang & Voke 2001; Chaurasia & Thompson 2011; Thompson 2012). Using flow visualization for a separation bubble at a blunt leading edge, Sasaki & Kiya (1991) reported that, in the range of $320 < Re < 380$, the shear layer rolls up to form aligned (in-phase) Λ-shape vortices shortly downstream of the reattachment line, whereas these are found to be in a staggered arrangement in the longitudinal direction for $Re > 380$; here Re is the Reynolds number based on the plate thickness. The numerical simulation of Yang & Voke (2001) reveals that the separated shear layer initially becomes unstable due to the Kelvin–Helmholtz (KH) instability and forms a two-dimensional (2-D) vortex followed by 3-D motions further downstream due to secondary instability, which eventually leads to a hairpin-like vortex before reattachment with the wall. In his transient growth analysis of this flow, Thompson (2012) found the optimal perturbation field to be localized near the leading edge. Interestingly, his analysis on the effect of noise reveals that a very small noise level (0.1 %) can lead a steady separation bubble to an unsteady one because of substantial amplification of optimal modes.

To investigate the response of FST on a separation bubble at the blunt leading edge of a flat plate, Hillier & Cherry (1981) carried out surface pressure measurements at various FST levels. They found that the mean flow strongly responds to FST, whereas unsteady characteristics strongly depend on both FST and integral scales. Similarly, Castro & Haque (1988) found enhancements of the flapping motion of a separated shear layer at an enhanced level of FST. A separation bubble generated by a rounded leading edge of a flat plate at an enhanced level of FST was also investigated by Stevenson *et al.* (2016), who found that laminar streaks co-exist with the shedding structure in the separated shear layer, and the shedding structure contributes to the Reynolds stress production in the rear part of the bubble.

Towards finding the frequency spectra, Halfon *et al.* (2004) carried out hot-wire measurements of a separation bubble formed near the leading edge of an elliptic flat plate for different levels of FST and periodic excitation. At low FST levels, clear peaks in the frequency spectra were observed, indicating the presence of the KH instability mechanism, whereas, for high FST cases, no clear peak was observed. Similarly, Langari & Yang (2013) reported that the faster growth of turbulence kinetic energy accelerates the transition process and bypasses the KH instability mechanism at a higher level of FST. In contrast, the numerical simulations of Yang & Abdalla (2005) and Yang & Abdalla (2009) reveal that the addition of FST does not alter the shedding frequency of the separated shear layer. This contrasting viewpoint on the existence of a peak in the spectra certainly invites further studies on the effect of FST on a GISB.

1.2. *Pressured-induced separation bubble*

As compared with the GISB cases, there have been considerable studies on the PISB cases, as Tani (1964) reviewed some early works on this subject. Various works on a PISB indicate that disturbance grows exponentially in the separated shear layer and eventually leads to the shear layer roll-up (e.g. Gaster 1967; Pauley, Moin & Reynolds 1990; Watmuff 1999; Häggmark, Bakchinov & Alfredsson 2000; Lang, Rist & Wagner 2004). Using the laser-Doppler anemometry and the particle image velocimetry (PIV) techniques, Lang *et al.* (2004) carried out a controlled experimental investigation in a PISB and compared their measured data with the linear stability theory and the direct numerical simulation. Their study reveals that transition is driven by a convective amplification of 2-D Tollmien–Schlichting (TS) waves, and the initial level of steady 3-D disturbances does not play a major role in the transition process. Similarly, for a separation bubble on an airfoil, Boutilier & Yarusevych (2012) found their measured growth rate,

wavenumber and convection velocity to compare well with the prediction of linear stability analysis (LSA). In their combined experimental and theoretical study, Diwan & Ramesh (2009) found that the primary instability mechanism in a separation bubble is inflectional in nature, which originates at the upstream of the separation location. They also proposed a new scaling relation for the most amplified frequency for a wall-bounded shear layer in terms of the inflection-point height and the vorticity thickness. Several studies (e.g. Spalart & Strelets 2000; Marxen *et al.* 2009; Marxen, Lang & Rist 2013) are also carried out to understand the 3-D aspect of the separated shear layer transition. In the case of a forced laminar separation bubble, Marxen *et al.* (2013) reported that an elliptic instability of the vortex core is responsible for the spanwise deformation, whereas a flow instability between two adjacent vortices is responsible for three dimensionality in the braid region.

Besides these controlled studies, the response of a separation bubble to an enhanced level of FST has also been investigated numerically and experimentally by various researchers. In his experimental work on the separation bubble under low-pressure turbine conditions at low (0.5 %) and high (9 %) FST levels, Volino (2002) found clear sharp spectral peaks for the low FST case, which led him to suggest TS instability mechanism for shear layer breakdown. For high FST levels, although he found the broadband spectrum, the peak was found to be at same the frequency as that of the low FST case, suggesting the possibility of TS transition even at high FST. Using the PIV technique, Simoni *et al.* (2017) carried out an experimental study on PISB for various Reynolds numbers and FST levels. They found that the vortex shedding frequency does not change considerably with increasing the FST level. Similarly, Istvan & Yarusevych (2018) experimentally studied the effects of FST on transition in a laminar separation bubble over a NACA 0018 airfoil using the PIV technique. They reported that the spanwise vortices originate from the shear layer roll-up for all the FST levels (0.06 %–1.99 %). However, they found that the spanwise coherence reduces significantly with increasing FST levels, and the streamwise streak of low-speed fluid at the highest level of FST (1.99 %) leads to highly 3-D shear layer roll-up.

In their numerical simulation, Balzer & Fasel (2016) found a constant shedding frequency at enhanced levels of FST and the vortex shedding is not bypassed in the flow. Furthermore, their study reveals that there exists the streamwise algebraic/transient growth in the fore part of the bubble, followed by an exponential growth; the streamwise algebraic growth is attributed to the streamwise streaks (Klebanoff mode, hereafter referred to as the K mode), whereas the exponential growth is due to the KH mode. Their LSA confirms that the primary linear stage of the transition mechanism (KH instability) is not bypassed even at an enhanced level of FST. A recent numerical study by Hosseinverdi & Fasel (2019) reveals that the K mode can emerge in the flow even at a smaller level of FST. Nevertheless, the transition is dominated by a 2-D mode (KH mode). When the FST level increases, both the K mode and the KH mode contribute to the transition mechanism. Similarly, in their large eddy simulation in a PISB in the presence of FST, Li & Yang (2019) reported that there exist two transition mechanisms, i.e. K-mode and KH-mode instability mechanisms. Their numerical flow visualization reveals that the spanwise 2-D rollers are severely distorted due to high FST, leading to highly 3-D rollers without any clear spectral peak associated with the KH instability. Nonetheless, the small peaks at different frequencies in their spectral analysis of the streamwise velocity data are reported to be associated with the shedding of the disrupted 2-D rollers, which may be a manifestation of the KH instability. However, they concluded that the KH instability mechanism is not the dominant mechanism at the FST level of 2.9 %. In their direct numerical simulation, McAuliffe & Yaras (2010) found that clear spectral peaks are absent in the bubble region at the FST level of 1.45 %. Moreover, they reported that the streamwise streaks in the

flow bypass the shear layer roll-up process, indicating that the primary KH instability mechanism leading to shear layer roll-up is bypassed, although they found this mechanism to be active at the secondary instability stage during turbulent spot formation.

1.3. *Aims of the present study*

The above reviews clearly indicate some contrasting observations on the presence of vortex shedding frequency and the instability mechanism in a separated shear layer at an enhanced level of FST. Some studies (e.g. Yang & Abdalla 2005, 2009; Balzer & Fasel 2016) indicate that the primary linear stage of the transition mechanism (KH instability) is not bypassed even at an enhanced level of FST, whereas some authors (e.g. McAuliffe & Yaras 2010; Langari & Yang 2013) concluded that the primary instability mechanism is bypassed, as they did not find any clear peak in the streamwise fluctuating velocity (u) spectra. An obvious question then is to ask: Can we come to a conclusion about the existence/non-existence of the primary instability mechanism based on the presence/absence of a spectral peak in the u velocity signal? If the spectral peak does not exist in the u velocity spectra or if it does not remain constant at an enhanced level of FST while other conditions remain the same, can the LSA even then describe the disturbance evolution in the separated flows?

Some works also reveal co-existence of both the K mode and KH mode in a separation bubble at an enhanced level of FST (e.g. Stevenson *et al.* 2016; Hosseinverdi & Fasel 2019; Li & Yang 2019). Then, another legitimate question which arises: Is this feature universal for all types of separation bubble? If both the K mode and KH mode are present, what role does the K mode/a streaky structure play in flow transition in a separated flow?

Therefore, the present comparative study is aimed at answering these above questions considering both the geometry-induced and pressure-induced separation bubbles. This paper is organized as follows. Details of the experimental set-ups and the measurement techniques are described in § 2, followed by the data analysis techniques in § 3. The results are presented in § 4. The summary of the results followed by a concluding remark is presented in § 5.

2. Experimental details

2.1. *Wind tunnels and set up for separation bubbles*

The present measurements were carried out in a low-turbulence and low-speed wind tunnel. The settling chamber of the open-return, suction-type wind tunnel houses a honeycomb section (30 mm long) and six turbulence reduction screens, followed by a contraction cone with a contraction ratio of 16 : 1. The tunnel has a square test section of dimensions 610 mm × 610 mm; the length of the test section is 3000 mm. The test section is followed by a long diffuser. A fan at the diffuser end is driven by a 15-hp motor, which is controlled by a speed controller (made by Siemens). The streamwise FST intensity in the empty test section is 0.1 % of the free-stream velocity (Balamurugan & Mandal 2017).

A transparent acrylic flat plate with a blunt leading edge (right-angled corners) was used for generation of a GISB (e.g. Hillier & Cherry 1981; Kiya & Sasaki 1983*a*), as schematically shown in figure 1(*a*). On the other hand, a contoured wall in the test section (e.g. Häggmark *et al.* 2000; Marxen *et al.* 2003; Diwan & Ramesh 2009), as shown in figure 1(*b*), was used to generate a PISB on a horizontal flat plate with an asymmetrical modified super elliptic leading edge. The present pressure gradient set-up is a slightly modified version of that used by Dhiman (2015). The contoured wall, which was made
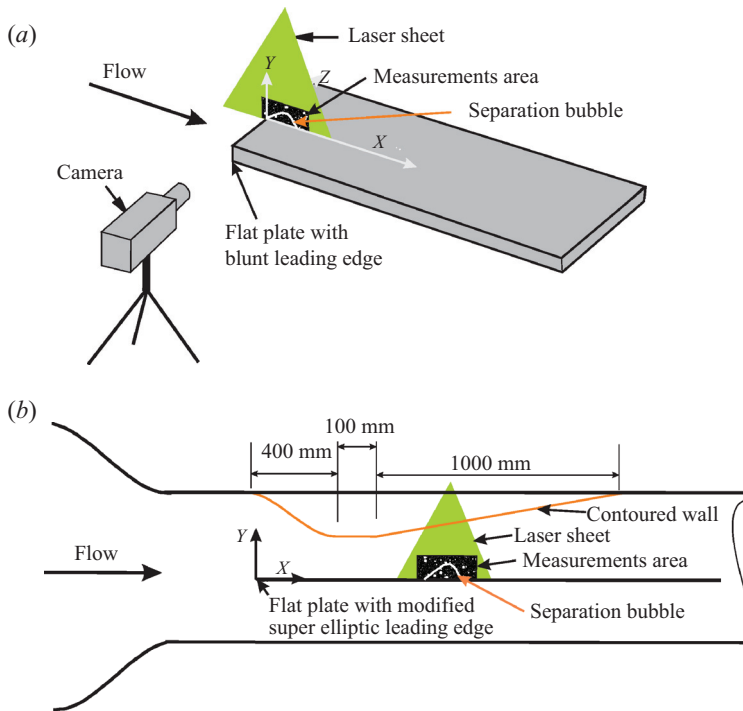
Figure 1. Simple sketches illustrating the arrangements for measurements in the wall-normal plane. (*a*) A blunt plate with right-angled corners for the generation of a GISB. (*b*) Contoured wall for generating a PISB over a flat plate with an asymmetric modified super elliptic leading edge.

of wood, was 1500 mm long and 610 mm wide with a maximum depth of 165 mm. The profile for the contoured wall in the favourable pressure gradient region was obtained from a fifth degree polynomial, $y_a = ax_a^5 + bx_a^4 + cx_a^3 + dx_a^2 + ex_a$, where a, b, c, d and e are constants. Here, the origin, i.e. $x_a = 0$ and $y_a = 0$, is located at the starting of the contoured wall from the top wall of the tunnel; x_a is positive in the flow direction, whereas y_a is positive upward. The numerical values of the constants a, b, c, d and e are -7.137×10^{-7}, 8.263×10^{-8}, -2.734×10^{-5}, 0.00158, -0.01324, respectively. Other portions of the contoured wall are straight lines. The boundary layer on the contoured wall was tripped to avoid flow separation on the contoured wall. A slot of 10 mm wide was made along the centreline of the contoured wall to facilitate the hot wire and the PIV measurements in the wall-normal plane. Both the plates were horizontally mounted in the mid-plane of the tunnel test section. The thickness of both the plates, denoted by h, was 12 mm. The plates with blunt and asymmetrical modified super elliptic leading edges were 1500 and 1800 mm long, respectively. The present asymmetric modified super elliptic leading edge was designed and fabricated following the work of Hanson, Buckley & Lavoie (2012), with a thickness ratio of 7/24 between the working and non-working sides. The leading edge was 120 mm long. The aspect ratios for the upper and lower ellipses were 34.3 and 14.1, respectively. Hanson *et al.* (2012) reported that this type of leading edge could reduce the receptivity of the boundary layer by eliminating the discontinuity at the juncture between the curved and the flat surfaces. Various studies in the literature considered flat plates with an asymmetric leading edge for reducing the pressure gradient around the leading edge region (e.g. Fransson, Matsubara & Alfredsson 2005; Li & Gaster 2006).

To increase the turbulence level in the test section, a passive grid was installed at the entrance of the test section. We used two different passive grids. These grids, denoted as grid A and grid B, were bi-plane square grids made of circular and square bars of mild steel, respectively. The diameter of the circular bars and the mesh width of grid A were 5 and 72 mm, respectively, whereas grid B was made of 10 thick square bars with 45 mm mesh width. The solidity of grid A was 0.134, whereas it was 0.39 for grid B. The turbulence generated by these grids was nearly isotropic. The streamwise turbulence intensities were found to be 2.1 % and 3.3 % for grid A and grid B, respectively, at the flat plate leading edge, which was approximately 20M downstream of the grid location; here M refers to the mesh width of a grid. The longitudinal integral length scales and the Taylor microscales were found to be 11.1 mm and 3.8 mm, respectively, for grid A, and 20.2 mm and 5.2 mm, respectively, for grid B. Further details, such as transverse integral length scales and the isotropic nature of the grid turbulence, are available in Aniffa (2023).

2.2. *Measurements techniques*

The PIV technique has extensively been used to measure the flow field in both the wall-normal (x–y) and spanwise (x–z) planes; here, the streamwise, wall-normal and spanwise directions are denoted by x, y and z, respectively, and the corresponding fluctuating velocities in those directions are denoted by $u = U - U_I$, $v = V - V_I$ and $w = W - W_I$, respectively, where the corresponding uppercase quantities without suffix I and with suffix I are the mean and instantaneous velocities, respectively. We may note that $x = 0$ refers to the origin of the leading edge of the flat plate. Measurements have been carried out using a conventional 2-D PIV system (data acquisition rate $\leq$ 10 Hz), and a time-resolved PIV (TR-PIV) system (data acquisition rate $\sim$1 kHz). Three different cameras were utilized in the present investigation. A high-resolution CCD camera (TSI, USA, 4912 $\times$ 3280 pixels, frame rate in double frame mode 1 Hz) was used for the conventional 2-D PIV system. Two different CMOS cameras, one with a resolution of 2560 $\times$ 1920 pixels (CMOS-1) and another with a resolution of 3840 $\times$ 2400 pixels (CMOS-2), were utilized in this work. Both of these cameras were procured from IDTvision, USA. The maximum frame rates at the maximum resolutions in double exposure mode are 365 and 500 Hz for the CMOS-1 and CMOS-2 cameras, respectively. It should be noted that all the TR-PIV measurements for the GISB and PISB cases were carried out using CMOS-1 and CMOS-2 cameras, respectively. A macro planner lens of 100 mm focal length (Carl Zeiss) was used with these cameras for data acquisition. Two laser units, i.e. a double pulsed Nd:YAG laser (InnoLas Laser GmbH, Germany, SpitLight Compact 400, energy 180 mJ per pulse at 532 nm, repetition rate 10 Hz), and a high-frequency double pulsed Nd:YLF laser (Photonics Industries, dual head DPSS, energy 30 mJ per pulse at 527 nm till the repetition rate of 1 kHz) were used for illumination. Using sheet forming optics and articulated light arms (procured from Laser and Imaging Sciences, UK, and ILA Intelligent Laser Applications GmbH, Germany), a thin laser sheet of approximately 1 mm thickness was produced and delivered to the measurement plane. The flow was seeded with fog particles of a mean diameter of approximately 1 μm using a fog generator (SAFEX fog generator, Dantec Dynamics, Denmark). It was placed ahead of the tunnel entrance, and a uniform distribution of fog particles was ensured using a small fan, as was done in our previous work in this tunnel (e.g. Balamurugan & Mandal 2017; Balamurugan *et al.* 2020). The laser and the camera were synchronized using the MotionPro timing unit (IDTpiv, USA) and the TSI synchronizer (TSI, USA). A simple sketch illustrating arrangements for the PIV

measurements in the *x*–*y* plane for both the GISB and PISB cases is shown in figures 1(*a*) and 1(*b*), respectively.

Before proceeding with the PIV measurements, the separation bubble region was identified using the smoke flow visualization technique. Since the separated region for a GISB was found to be comparatively small, the CMOS camera was used for both the conventional and the TR-PIV measurements with regions of interest in the (*x*–*y*) plane of 113 mm × 85 and 100 mm × 42 mm, respectively; we may note that the region of interest for the TR-PIV measurements was chosen to be less than the conventional measurements to increase the acquisition rate. Similarly, the conventional and TR-PIV measurements were carried out for a PISB in the (*x*–*y*) plane. As the separated region was found to be large in a PISB, a high-resolution CCD camera was used to cover 310 mm × 207 mm in the (*x*–*y*) plane for better spatial resolution. On the other hand, the TR-PIV measurements in the (*x*–*y*) plane for a PISB were carried out covering 158 mm × 89 mm around the maximum height of the bubble for the comparable spatial resolution. The conventional PIV measurements using the CCD camera in the (*x*–*z*) plane were also carried out at $y = 2$ mm height from the surface, for both the GISB and PISB cases, with regions of interest of 201 mm × 134 mm and 258 mm × 172 mm, respectively. Sufficient numbers of realizations were acquired for both the PISB and GISB cases, as detailed in the following section. The TR-PIV data were acquired at 645 Hz, i.e. 645 image pairs per second, for the GISB cases, whereas the TR-PIV data were acquired at 500 Hz for the PISB case. Similarly, the conventional measurements were acquired at a rate of 1 Hz, except for the conventional measurements in the (*x*–*y*) plane for a GISB, which were carried out at a rate of 10 Hz. However, the acquired images were processed using the mess-free software, ProVision XS (IDTpiv), with a correlation window of 32 pixels × 32 pixels. The package, ProVision XS, includes a feature for high spatial resolution, details of which can be found in the literature (Lourenco & Krothapalli 2000; Alkislar, Krothapalli & Lourenco 2003). This package was also used in various previous works (e.g. Mandal, Venkatakrishnan & Dey 2010; Balamurugan & Mandal 2017). The uncertainty analysis of the PIV measurements was performed following our previous work (Balamurugan & Mandal 2017). We considered the uncertainty due to particle displacement, alignment of the calibration target and time delay of the signal (Gui & Wereley 2002; Holman 2012; Thielicke 2014; Coleman & Steele 2018; Raffel *et al.* 2018). The estimated maximum uncertainties in the velocity are found to be $\pm 1.5\%$ and $\pm 2.6\%$ of the free-stream velocity for the GISB and PISB cases, respectively. A hot-wire anemometry system procured from Dantec Dynamics, Denmark, was also used in this present study. A single hot-wire probe (55P11, Dantec Dynamics) was used for data acquisition. The sensing element was 5 µm diameter tungsten wire with a length to diameter ratio of 250. The data were acquired using a 16 bit NI data acquisition card and the LabVIEW software with a sampling rate of 6 kHz. For measuring the free-stream turbulent intensity, the probe was calibrated using a Pitot static tube and the King's law fit. The uncertainty in the mean velocity measured by the hot-wire system is estimated following the works of Yavuzkurt (1984) and Balamurugan & Mandal (2017). The estimated uncertainty is found to be less than $\pm 2.5\%$.

2.3. *Velocity and pressure distributions*

The coefficient of pressure, C_p $(= 1 - (U_e^2 + V_e^2)/U_r^2)$, for the GISB cases, was determined from the streamwise edge velocity (U_e) and the wall-normal edge velocity (V_e) of the separated shear layer, whereas the coefficient of pressure, Cp $(= 1 - U^2/U_r^2)$, for the PISB cases were determined from the mean velocity measured outside of the
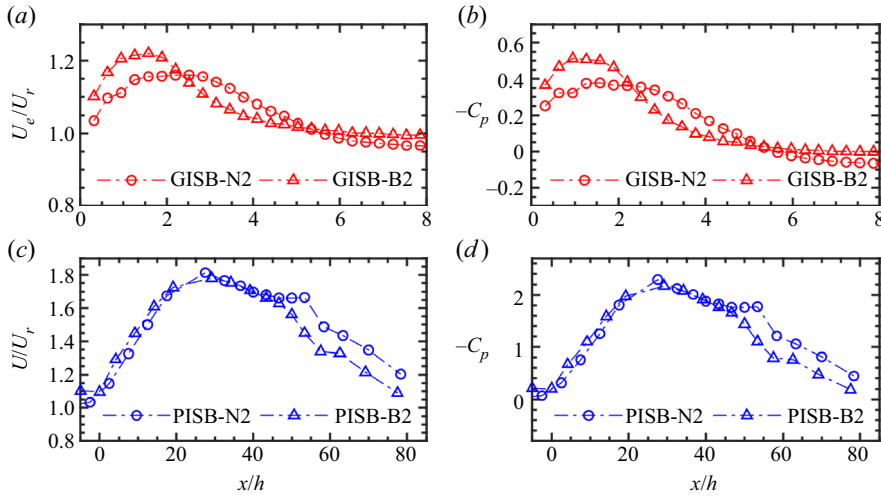
Figure 2. (*a,b*) Plots of U_e/U_r and C_p distributions along the streamwsie direction, respectively, for different GISB cases. Symbols: $--\circ--$, red, GISB-N2 case; $--\triangle--$, red, GISB-B2 case. (*c,d*) Plots of U/U_r and C_p distributions along the streamwsie direction, respectively, for different PISB cases. Symbols: $--\circ--$, blue, PISB-N2 case measured at $y/h = 1.25$; $--\triangle--$, blue, PISB-B2 case measured at $y/h = 0.5$; here GISB-N2 and GISB-B2 refer to measurements at $U_r = 2$ m s^{-1} for no grid and grid B, respectively, for the GISB cases; PISB-N2 and PISB-B2 refer to measurements at $U_r = 2$ m s^{-1} for no grid and grid B, respectively, for the PISB cases, as further detailed in table 1.

separation bubble; here, the reference velocity, U_r, is considered as the mean velocity at $x = -220$ mm from the plate leading edge, such that this location is well ahead of the converging section of the contoured wall, and the edge velocity, U_e, is considered as the mean velocity at the shear layer edge. However, for the GISB cases, U_e and V_e were obtained from the PIV measurements in the wall-normal plane. For the PISB cases, such PIV measurements over the entire length of the pressure gradient set-up were not possible. Therefore, the hot-wire measurements were carried out to determine the mean velocity for the PISB cases. The measurements were carried out at various streamwise locations while keeping the probe at a wall-normal location higher than the maximum height of a PISB. The hot-wire data were acquired at a rate of 6 kHz.

Variations of U_e/U_r and C_p distributions along the streamwise direction are shown in figures 2(*a*) and 2(*b*), respectively, for the GISB cases. Similarly, figures 2(*c*) and 2(*d*) show U/U_r and C_p distributions, respectively, for the PISB cases. It should be noted that GISB-N2 and GISB-B2 in these figures denote measurements with no grid and grid B at $U_r = 2$ m s^{-1} for the GISB cases; similarly, PISB-N2 and PISB-B2 denote measurements with no grid and grid B at $U_r = 2$ m s^{-1} for the PISB cases; the hot-wire measurements along the streamwise direction were carried out keeping the hot-wire probe at $y/h = 1.25$ and $y/h = 0.5$ for the PISB-N2 and PISB-B2 cases, respectively. The flow for the GISB cases is seen to accelerate initially before it decelerates in the downstream, although the flow separates at the blunt leading edge (with right-angled corners). Furthermore, the increase in the edge velocity is found to be more for an enhanced level of FST, i.e. for the GISB-B2 case as compared with the GISB-N2 case. This is attributed to the fact that the mean velocity around the point of separation is no more parallel to the streamwise direction, as the flow separates at an angle at the corner of the blunt leading edge (see figure 3 in § 4). This leads to the non-zero value of the wall-normal mean velocity, V,
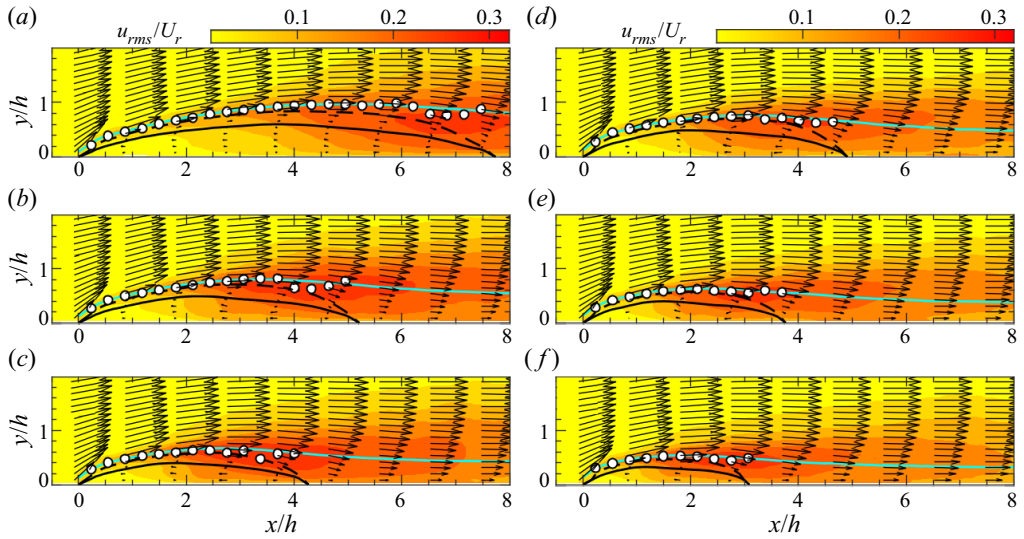
Figure 3. Ensemble-averaged velocity vectors plotted over the contour of u_{rms}/U_r. Symbols: —, $U = 0$ line; – – –, mean dividing streamline; ——, cyan, displacement thickness (δ^*); ○, location of the inflection points. Results are shown for the (*a*) GISB-N1 case, (*b*) GISB-A1 case, (*c*) GISB-B1 case, (*d*) GISB-N2 case, (*e*) GISB-A2 case, (*f*) GISB-B2 case.

which is found to be higher for the GISB-N2 case as compared with the GISB-B2 case. As a result, the streamwise component of the mean velocity, i.e. U_e, is found to be less for the GISB-N2 compared with the GISB-B2 case for a given reference velocity, $U_r = 2$ m s^{-1}. For the PISB cases, the flow in the converging section of the contoured wall accelerates as expected, followed by a deceleration in the diverging section. Moreover, the streamwise distributions of U/U_r and C_p for the PISB-N2 and PISB-B2 cases are nearly similar before the point of separation, as the mean flow is nearly parallel (see figure 4 in § 4). The U/U_r variation in figure 2(*c*) is found to be similar to the velocity distribution reported in the literature (e.g. Häggmark *et al.* 2000; Li & Yang 2019; Coull & Hodson 2011) for the PISB cases. The sudden drop in the value of C_p in the range of $50 < x/h < 60$ in figure 2(*d*) indicates the transition in the separated shear layer (e.g. Häggmark *et al.* 2000; Boutilier & Yarusevych 2012; Balzer & Fasel 2016).

3. Data analysis techniques

In this section we briefly describe the major data analysis tools, i.e. the proper orthogonal decomposition (POD) and LSA techniques.

3.1. *The POD technique*

The POD technique provides a set of orthogonal basis functions, $\boldsymbol{\Phi}(x)$, which can be used to decompose the fluctuating velocity field, $\boldsymbol{v}(x)$, as follows (Baltzer & Adrian 2011; Berkooz, Holmes & Lumley 1993):

$$\boldsymbol{v}(\boldsymbol{x}, t_m) = \sum_n a^n(t_m)\boldsymbol{\Phi}^n(\boldsymbol{x}). \tag{3.1}$$
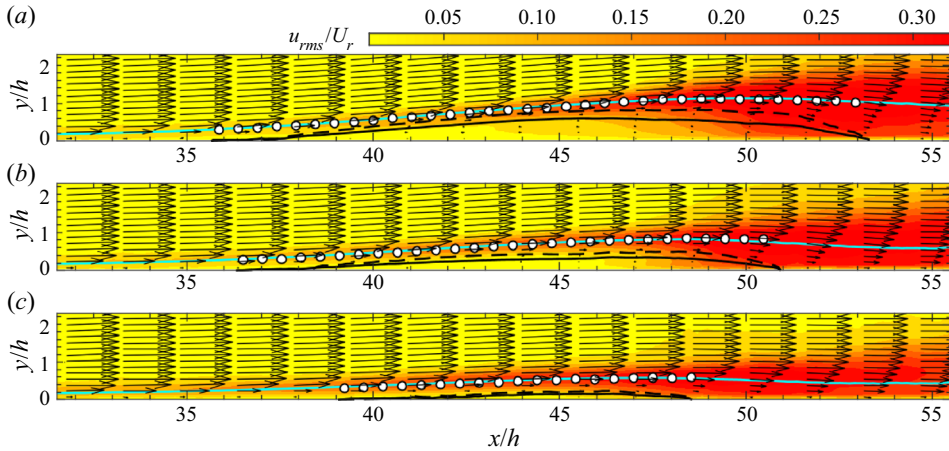
Figure 4. Ensemble-averaged velocity vectors plotted over the contour of u_{rms}/U_r for PISB cases. Symbols: —, $U = 0$ line; – – –, mean dividing streamline; ——, cyan, displacement thickness (δ^*); ∘, location of the inflection points. Results are shown for the (a) PISB-N2 case, (b) PISB-A2 case, (c) PISB-B2 case.

Here the coefficients, $a^n(t_m)$, can be obtained by the following inner product:

$$a^n(t_m) = (v(x, t_m), \Phi^n(x)). \tag{3.2}$$

The basis function, $\Phi(x)$, to be an optimum one, should satisfy the following integral eigenvalue equation (Berkooz *et al.* 1993):

$$\int_\Omega R(x; x')\Phi(x')\, dx' = \lambda\Phi(x). \tag{3.3}$$

Here $R(x; x') = \langle v(x)v^*(x')\rangle$ represents a two-point correlation and Ω denotes the domain of integration. The normalized basis functions are obtained such that $(\Phi^m, \Phi^n) = \delta_{mn}$, where δ_{mn} is the Kronecker delta.

Using 'the method of snapshot' proposed by Sirovich (1987), POD basis functions are usually calculated from discrete PIV data (e.g. Kruse, Gunther & Rohr 2003; Meyer, Pedersen & Özcan 2007; Mandal *et al.* 2010). Following Mandal *et al.* (2010), a covariance matrix, defined as $R_{ij} = (C_i, C_j)$, where C_i contains a fluctuating velocity field from a PIV snapshot, is formed. Using the eigenvectors (ϕ_i) of the covariance matrix, POD modes are defined as

$$\Phi^n = \sum_{i=1}^N \phi_i^n C_i, \quad n = 1, \ldots, N. \tag{3.4}$$

Here N indicates the total number of PIV snapshots. Similarly, using the eigenvalues (λ_i) of the covariance matrix, relative energy is defined as $E_n = \lambda_n/\sum_1^N \lambda_i \times 100\,\%$.

3.2. *The LSA technique*

The stability of a base flow to a small amplitude perturbation, under the parallel flow approximation, is governed by the Orr–Sommerfeld equation (OSE), as detailed in various books (e.g. Schmid & Henningson 2001; White 2006). Following Boutilier &

Yarusevych ([2012](#)) and Balamurugan & Mandal ([2017](#)), the OSE can be expressed as

$$(\alpha U - \omega)\,[\hat{v}'' - \alpha^2 \hat{v}] - \alpha U'' \hat{v} = -\frac{\mathrm{i} U_e \theta}{Re_\theta}[\hat{v}'''' - 2\alpha^2 \hat{v}'' + \alpha^4 \hat{v}], \qquad (3.5)$$

where $\hat{v}$ is the complex amplitude of the vertical disturbance velocity, i.e. $v = \hat{v}\mathrm{e}^{\mathrm{i}(\alpha x - \omega t)}$, and its differentiation with respect to the wall-normal distance is denoted by $\hat{v}'$; here α, ω and $Re_\theta(= U_e\theta/\nu)$, respectively, denote the wavenumber, the angular frequency and the Reynolds number based on the boundary layer edge velocity, U_e, and the momentum thickness, θ. We may mention that the edge velocity, U_e, is defined here as the maximum streamwise velocity in the free-stream side of a separated shear layer. Using the disturbance continuity equation, one can find the amplitude function of the streamwise disturbance velocity, $\hat{u}(= \mathrm{i}\hat{v}'/\alpha)$. The boundary conditions for the (3.5) for the boundary layer flows are $\hat{v}(0) = \hat{v}(\infty) = 0$ and $\hat{v}'(0) = \hat{v}'(\infty) = 0$. Similarly, for inviscid stability analysis in the limit of $Re \to \infty$, we consider the Rayleigh equation

$$(\alpha U - \omega)\,[\hat{v}'' - \alpha^2 \hat{v}] - \alpha U'' \hat{v} = 0, \qquad (3.6)$$

with the boundary conditions, $\hat{v}(0) = \hat{v}(\infty) = 0$. Considering the wavenumber, $\alpha = \alpha_r + \mathrm{i}\alpha_i$, as complex and the angular frequency, ω, as real, both (3.5) and (3.6) can be solved using the spectral collocation method based on Chebyshev polynomials for a given velocity profile at a given Reynolds number (see Schmid & Henningson [2001](#); Dabaria [2015](#), for further details). To determine the most amplified frequency, the spatial growth rates, $-\alpha_i$, are usually calculated at various angular frequencies, ω, for a given velocity profile and Reynolds number (e.g. Dovgal *et al.* [1994](#); Boutilier & Yarusevych [2012](#)).

4. Results and discussions

For each separation bubble, measurements in the *x–y* and *x–z* planes with and without a particular grid in the tunnel test section were carried out at a constant reference velocity, U_r, in the free stream. The reference location at $x = -220$ mm from the leading edge of the flat plate was chosen such that it was well ahead of the converging section of the contoured wall, as already mentioned. A constant reference velocity with and without a grid in the test section was achieved by adjusting the rotational speed of the fan. This is necessary as the presence of a grid in the test section reduces the free-stream velocity due to a pressure drop across the grid. Whole field PIV measurements were carried out using the conventional PIV and TR-PIV techniques for all the GISB and PISB cases reported in this paper. The details of the measurement field of views of the GISB and PISB cases are given in § [2.2](#). For GISB cases, measurements were carried out for two reference velocities, (i.e. at $U_r = 1$ and 2 m s^{-1},) and for PISB cases, measurements were carried out at only one reference velocity (i.e. at $U_r = 2$ m s^{-1} and the corresponding Reynolds number based on the plate length, $U_r L/\nu = 1.91 \times 10^5$). Several cases considered in this study are detailed in table [1](#), along with the pressure gradient parameter and the Reynolds number at the point of separation. Using the criterion of the pressure gradient parameter, $P(= (y_{d,max}^2/\nu)(\triangle U/\triangle X)) > -28$ for a short bubble, as proposed by Diwan, Chetan & Ramesh ([2006](#)), we find that the present PISB cases are short bubbles as $P > -28$. Here, $\triangle U$ and $\triangle X$ denote the velocity difference and spatial distance between reattachment and the separation point, respectively; the height of the mean dividing streamline from the wall, y_d, is determined using the equation $\int_0^{y_d} U\,\mathrm{d}y = 0$ (Fitzgerald & Mueller [1990](#)), and the displacement thickness, δ^*, is estimated based on the shear layer edge velocity, U_e.

Cases	Grid and U_r (m s^{-1})	Re $\left(\dfrac{U_r h}{\nu}\right)/\left(\dfrac{U_r L}{\nu}\right)$	$Re_{\delta^*,s}/Re_{\theta,s}$ $\left(\dfrac{U_e\delta^*}{\nu}\right)_s /\left(\dfrac{U_e\theta}{\nu}\right)_s$	P	N_{PIV} x–y/x–z plane	N_{TR-PIV} x–y/x–z plane	Symbols
GISB-N1	No grid (1)	764/9.55×10⁴	63/32	—	800/430	—	◯
GISB-A1	Grid A (1)	764/9.55×10⁴	84/39	—	800/430	—	□
GISB-B1	Grid B (1)	764/9.55×10⁴	91/42	—	800/430	—	△
GISB-N2	No grid (2)	1529/1.91×10⁵	181/80	—	800/430	1400/—	◯
GISB-A2	Grid A (2)	1529/1.91×10⁵	191/83	—	800/430	—	□
GISB-B2	Grid B (2)	1529/1.91×10⁵	199/87	—	800/430	1400/—	△
PISB-N2	No grid (2)	1529/2.29×10⁵	966/245	−13.6	1000/600	1750/1750	◯
PISB-A2	Grid A (2)	1529/2.29×10⁵	924/253	−4.8	1000/600	—	□
PISB-B2	Grid B (2)	1529/2.29×10⁵	1021/278	−0.95	1000/600	1750/1750	△

Table 1. Details of various cases considered. Here N_{PIV} refers to the number of conventional PIV realizations and N_{TR-PIV} refers to the number of TR-PIV realizations. The reference velocity (U_r) for each case in m s^{-1} is indicated inside the parenthesis of the second column. Here $P(=(y_{d,max}^2/\nu)(\Delta U/\Delta X))$ is the pressure gradient parameter.

The symbols used for various cases in this paper are also given in this table, and an exception to this will be mentioned in the text. In the following, the plate thickness, h, and the reference velocity, U_r, have often been used as the length and velocity scales for normalization.

4.1. *Mean flow characteristics*

Mean flow characteristics for various cases, as mentioned in table 1, are obtained based on the ensemble average of the PIV realizations acquired using the conventional PIV system. Mean velocity vectors overlaid with the contours of u_{rms}/U_r are shown in figures 3 and 4 for various GISB and PISB cases, respectively. One may notice in figures 3 and 4 that the maximum value of u_{rms}/U_r occurs in the downstream region of the maximum height of a separation bubble. Similar to u_{rms}/U_r values, v_{rms}/U_r values are also found to be higher in this region (not shown here for brevity). This can be attributed to the transition-to-turbulent activity in the separated shear layer. These figures also show that the size of a separation bubble (i.e. both length and height) reduces with increasing FST intensity and Reynolds numbers, as can be deduced from the $U = 0$ line and the mean dividing streamline for both the GISB and PISB cases. These experimental observations for the present PISB cases are found to be similar to the recent numerical works of Balzer & Fasel (2016) and Hosseinverdi & Fasel (2019), among others. In addition, the present measurements reveal that the distance between the point of separation and the streamwise location of the maximum height of a separation bubble obtained based on the mean dividing streamline is large, as compared with the distance obtained based on the $U = 0$ line, as can be seen in these figures. Interestingly, we also find that the distance of the location of the point of inflection in the velocity profile from the wall is equal to the numerical value of the displacement thickness, as can be seen in figures 3 and 4.

The mean velocity vectors in figures 3 and 4 also indicate that there exists a point of inflection in the mean velocity profile within the separated region, as expected. The ratio of the mean velocity at the point of inflection, U_{in}, and the edge velocity, U_e, as shown in figure 5, is found to be nearly constant for all the cases considered here. In fact, some published data (Häggmark *et al.* 2000; Balzer & Fasel 2016; Hosseinverdi & Fasel 2019), also reveal that this is indeed correct. Here, x_s and $l_b(= x_r - x_s)$ denote the point of separation and the streamwise length of a separation bubble, respectively; x_r denotes the point of reattachment. We may note that we have followed the procedure of Häggmark (2000) to find the numerical values of x_s and x_r at the wall. It should be further noted that the point of inflection is estimated based on the different curve fits to the experimental data, and the error bars, as shown in figure 5, indicate one standard deviation with respect to the mean values of U_{in}/U_e, obtained using different curve fits. The ratio, $U_{in}/U_e \approx 0.5$, appears to remain unaffected by the FST levels at least up to 3.3 % for both the GISB and PISB cases.

For better comparison and to be more specific regarding the bubble dimensions, the $U = 0$ line and the mean dividing streamline, respectively, are shown in figures 6(*a*,*b*) and 6(*c*,*d*) for various GISB and PISB cases, respectively; the numerical values of the point of separation, the maximum height and the reattachment point are detailed in the table 2. These figures clearly show that the bubble height is reduced, and the point of reattachment is shifted towards the leading edge with an increasing level of FST. Without enhancing the FST level, reduction in bubble size is also observed with increasing *Re* (see the GISB-N1 and GISB-N2 cases in figure 6*a*,*b*). However, in contrast to the PISB cases (figure 6*c*,*d*), the point of separation and the bubble outline remain unchanged nearly up to the maximum height of the bubble for the GISB cases with increasing FST and

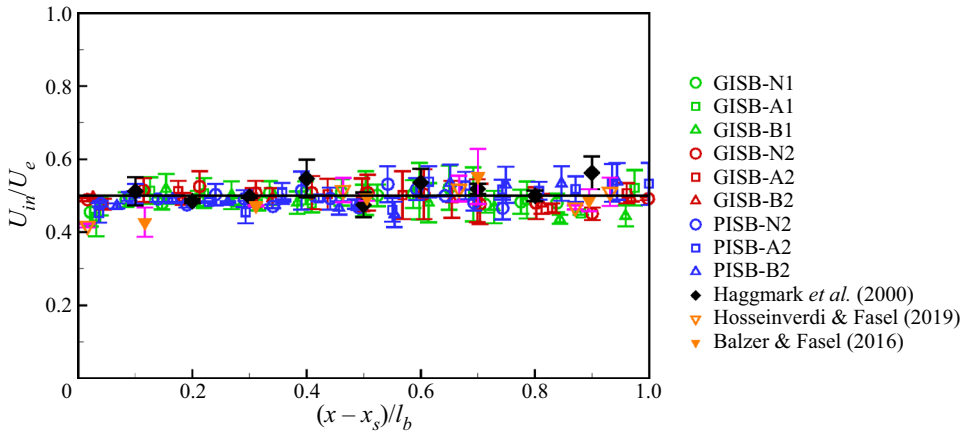Figure 5. Ratio of the mean velocity at the point of inflection, U_{in}, and the shear layer edge velocity, U_e, for different cases. Ratios determined from the data of Häggmark *et al.* (2000), Hosseinverdi & Fasel (2019) and Balzer & Fasel (2016) are also shown in this figure.

Re, as seen in figure 6(*a,b*). This can be attributed to the fact that the free-stream flow with different levels of FST does not contain any streaky structures and separates at the leading edge for the GISB cases, whereas the attached boundary layer that can be laden with streaky structures based on the level of FST separates from the wall for the PISB cases, as shown and discussed in § 4.4. Therefore, initially, the bubble outline for the GISB cases remains the same, but it changes later on due to the rapid transition-to-turbulent process in the separated shear layer triggered by a high level of FST. On the other hand, the transition-to-turbulent characteristics in the separated shear layer for the PISB cases depend not only on the different levels of FST but also on the nature of the attached boundary layer getting separated due to an adverse pressure gradient. Another contrasting observation between the GISB and PISB cases is that the ratio of the bubble length to its maximum height is approximately constant for the GISB cases, whereas this ratio is found to increase for the PISB cases with an increasing FST level (see table 2).

To investigate the self-similar nature of the bubble outlines, the streamwise and wall-normal coordinates of the $U = 0$ line and the mean dividing streamline are normalized by the respective bubble length and the maximum height, as shown in figures 6(*e*) and 6(*f*) for the GISB cases, and in figures 6(*g*) and 6(*h*) for the PISB cases, respectively. One may notice that the bubble outline in terms of the mean dividing streamline shows a better collapse of the data for both the GISB and PISB cases (see figures 6*f* and 6*h* in comparison with figures 6*e* and 6*g*, respectively). An exact collapse of the data for the mean dividing streamline is found for the GISB cases, whereas a small deviation may be seen for the PISB cases. In fact, a similar collapse of the data for the $U = 0$ line and the mean dividing streamline for various levels of FST for PISBs are also found for the experimental and numerical data of Simoni *et al.* (2017) and Balzer & Fasel (2016), as shown in figures 6(*i*) and 6(*j*), respectively.

To investigate the nature of disturbance growth in a separation bubble, variations of the normalized peak u_{rms} and the peak v_{rms} in the streamwise direction are shown in figure 7. One may clearly notice an exponential growth regime exists for all the cases considered here. At the initial stage after separation for the GISB cases, there is a jump in the growth of $u_{rms,max}/U_r$, as seen at approximately $x/h = 0.5$–1 in figure 7(*a,b*). This is found to be
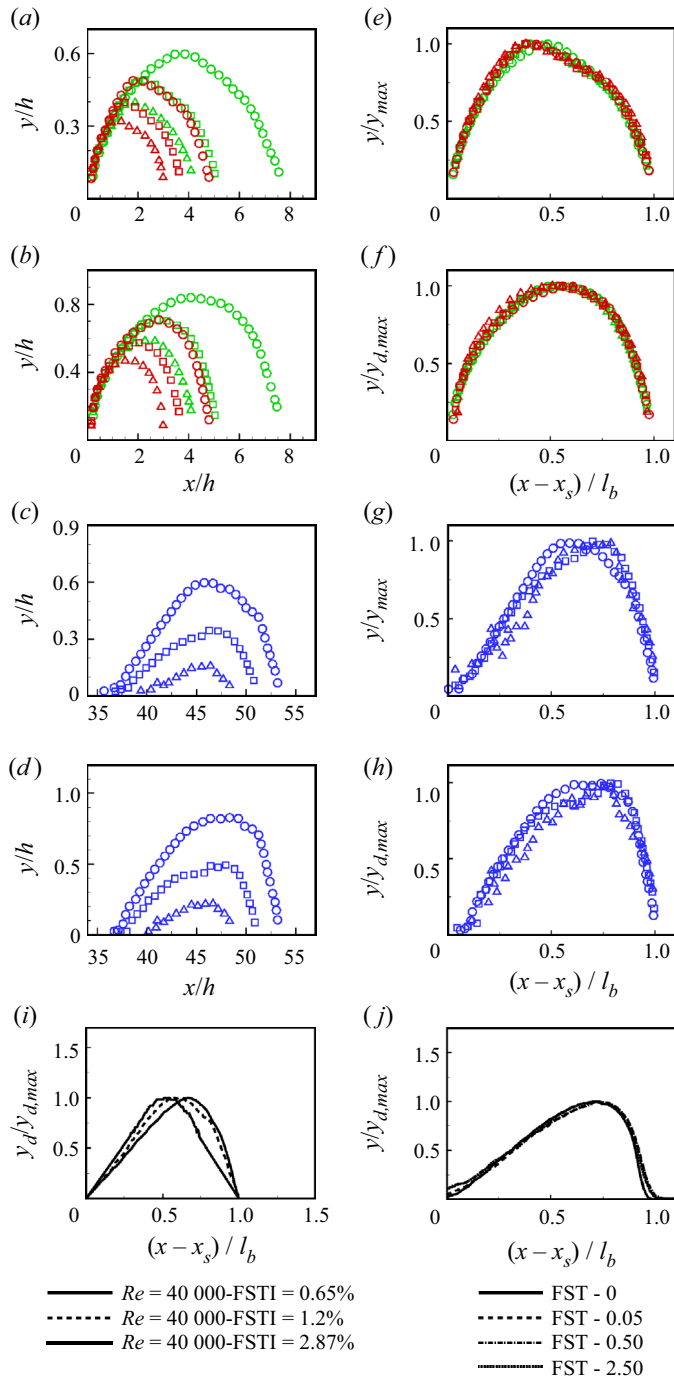
957 A19-15

Figure 6. Comparison of the $U = 0$ line and the mean dividing streamline for various cases considered and their self-similar characteristic. Descriptions of symbols used in this figure are detailed in table 1. (*a*,*b*) The $U = 0$ line and the mean dividing streamline, respectively, for various GISB cases. (*c*,*d*) The $U = 0$ line and the mean dividing streamline, respectively, for various PISB cases. (*e*,*f*) Self-similar characteristics of the $U = 0$ line and the mean dividing streamline, respectively, for various GISB cases. (*g*,*h*) Self-similar characteristics of the $U = 0$ line and the mean dividing streamline, respectively, for various PISB cases. (*i*) Self-similar characteristics of the $U = 0$ line for the data of Simoni *et al.* (2017). (*j*) Self-similar characteristics of the mean dividing streamline for the data of Balzer & Fasel (2016).

957 A19-16

Cases	Point of separation (x_s/h)	Point of reattachment (x_r/h)	Maximum height (y_{max}/h)	Ratio of length to y_{max} (l_b/y_{max})	Ratio of length to $y_{d,max}$ ($l_b/y_{d,max}$)
GISB-N1	0	7.74	0.60	12.89	9.22
GISB-A1	0	5.21	0.49	10.61	7.34
GISB-B1	0	4.27	0.40	10.72	7.23
GISB-N2	0	4.91	0.49	10.02	6.94
GISB-A2	0	3.76	0.40	9.45	6.55
GISB-B2	0	3.09	0.33	9.47	6.58
PISB-N2	35.65	53.30	0.60	29.32	21.20
PISB-A2	36.32	50.94	0.35	41.86	29.26
PISB-B2	39.06	48.56	0.16	60.09	39.62

Table 2. Various parameters of a separation bubble for different cases considered. Here, x_s, x_m, x_r, y_{max} and l_b indicate point of separation, streamwise location of the maximum height, point of reattachment, the maximum height based on $U = 0$ line and the length of a separation bubble, respectively. Large variation of l_b/y_{max} may be noted for the PISB cases, as compared with the GISB cases.
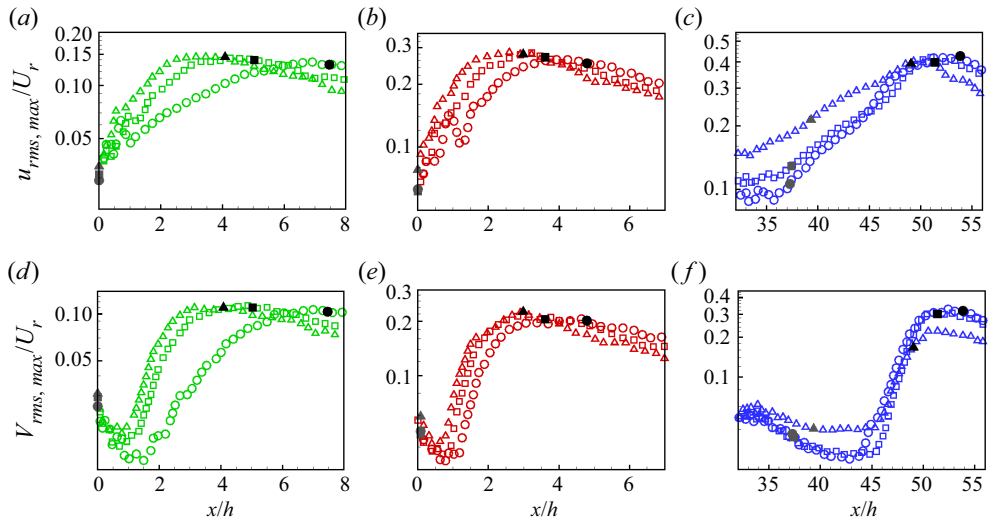
Figure 7. Streamwise variation of $u_{rms,max}/U_r$ and $v_{rms,max}/U_r$ for GISB cases (a,b,d,e) and PISB cases (c,f). Description of symbols is given in table 1. Separation and reattachment points for each case are shown by filled grey and black coloured symbols, respectively.

due to the presence of small shear layer vortices near to the blunt leading edge of the flat plate (see figure 8a,b, for example).

The exponential growth of $v_{rms,max}/U_r$ in figure 7(d–f) is attributed to the significant increase of the v fluctuation due to the vortex shedding associated with the separated shear layer. That is, the rapid increase of $v_{rms,max}/U_r$ can be considered as the starting location of the shear layer roll-up/vortex shedding. Kirk & Yarusevych (2017) also observed that the shear layer roll-up location is near to a point where the pressure fluctuation increases rapidly. Moreover, figure 7(d,e) shows that the onset of the exponential growth is shifted towards the leading edge under the high level of FST for the GISB cases, whereas the onset of the exponential growth is delayed and shifted in the downstream direction for the PISB cases, as seen in figure 7(f). This is because of the fact that the presence of a high level of initial disturbance in the free-stream flow leads to the rapid transition and shear layer roll-up for the GISB cases. On the other hand, the streaky structures are generated at an enhanced level of FST in the attached boundary layer prior to its separation for the PISB cases (as shown and discussed in § 4.4). These streaky structures delay the flow separation (e.g. Dellacasagrande *et al.* 2020; Karp & Hack 2020; Xu & Wu 2021).

4.2. *Unsteady flow characteristics in wall-normal (x–y) plane*

The growth of disturbance in a separated shear layer eventually leads to the roll-up of the shear layer into a vortex that detaches from the shear layer and initiates vortex shedding at some downstream distance from the point of separation (e.g. Pauley *et al.* 1990; Watmuff 1997). To investigate the detailed shedding characteristics of these vortices, the TR-PIV measurements were carried out in the wall-normal plane for both the GISB and PISB cases. Time sequences of such vortex shedding with and without an enhanced level of FST are shown in figure 8 for both the GISB and PISB cases. The displacement thickness curve denoted by a dashed line is seen to pass through the concentrated vorticity region for all the cases shown here. This indicates that the locus of the cores of shed vortices can
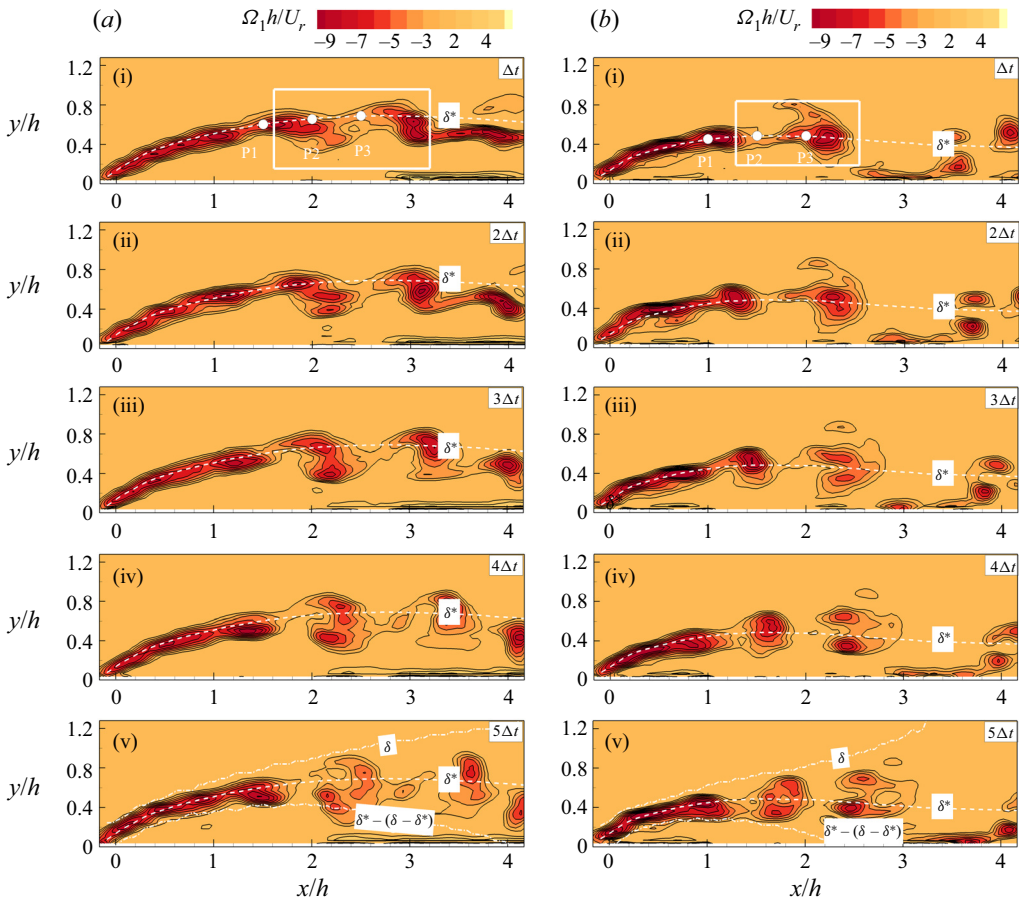
957 A19-18

Figure 8. For caption see next page.

be described by the displacement thickness curve, on an average. Unlike the PISB cases, the vorticity contours for the GISB-N2 and GISB-B2 cases indicate the presence of small vortices near the leading edge of the flat plate and large-scale vortices near the maximum height of the bubble (see the rectangular zone). The presence of such small vortices near the leading edge of a square cylinder is also reported by Brun *et al.* (2008), who call these small-scale vortices the KH vortices. For the present GISB cases, the separated shear layers containing such small vortices near the leading edge are called shear layer vortices. Figure 8(*a,b*) show that these small vortices eventually rolls up into large vortices near the maximum height of the bubble, which are referred to here as the shedding vortices.

Figure 9 shows the spectral analyses of *u* and *v* velocities at three different points (P1, P2, P3), as shown by white coloured solid symbols in figure 8. Figures 9(*a–d*) and 9(*e–h*) show the frequency spectra for *u* and *v* velocities, respectively. It should be noted that the frequency, *f*, has been normalized as $f^* = fh/U_r$, and as $F^* (= 2\pi f \nu / U_r^2 \times 10^6)$, where ν is kinematic viscosity of air. Figure 9 shows that the spectral analysis of *v* velocity signal can clearly identify the underlying dominant peaks, as compared with the spectral analysis of *u* velocity signal.

The dominant spectral peaks at points P1 and P2 for both the GISB-N2 and GISB-B2 cases are found to be 0.59, whereas the dominant peaks at point P3 for these cases are
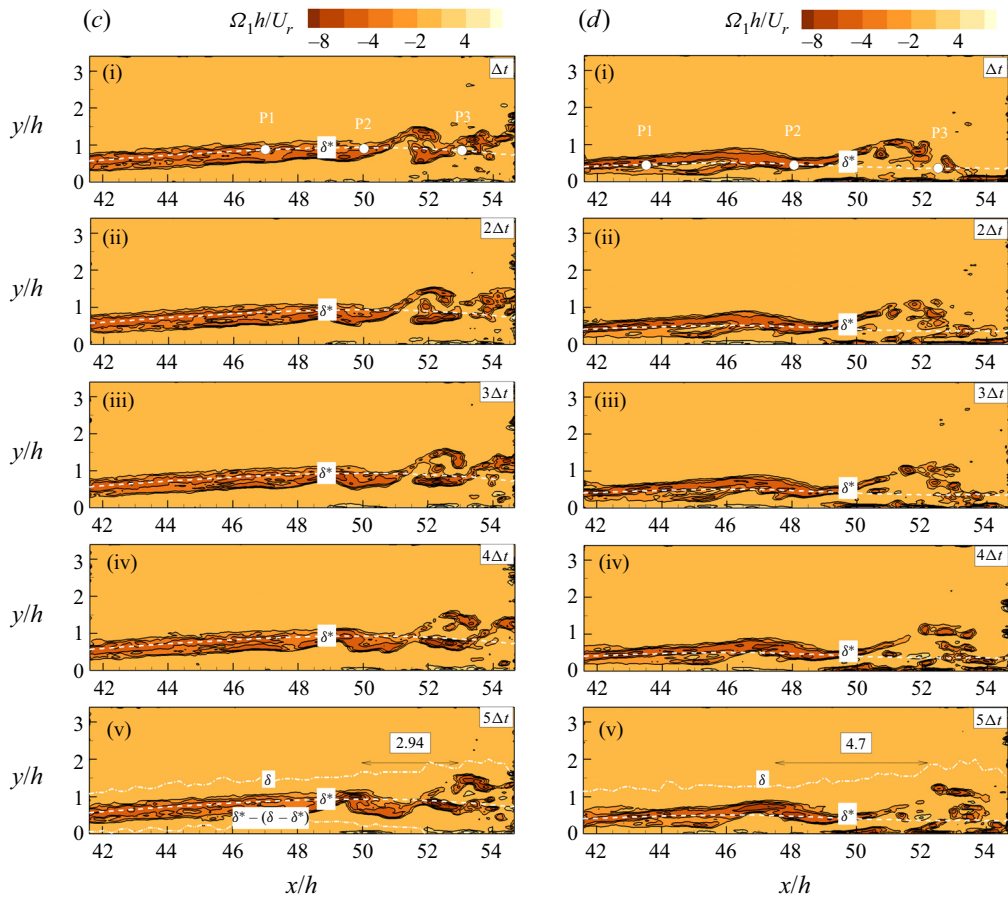
957 A19-19

Figure 8 (cntd). Time sequence of the roll-up process and vortex shedding in terms of the spanwise vorticity contours for various cases. Results are shown for the (*a*) GISB-N2 case, (*b*) GISB-B2 case, (*c*) PISB-N2 case, (*d*) PISB-B2 case.

found to be 0.38, as clearly seen in figure 9(*e*, *f*). The peak at 0.59 is attributed to the presence of the shear layer vortices, as discussed above, and the peak at ≈0.38 is due to the shedding vortices. It is interesting to note that the peaks associated with both the shear layer vortices and the shedding vortices are not changed even at an enhanced level of FST for the GISB cases. Dominant shedding frequencies and the Strouhal number (St_θ) based on θ and U_e at the point of separation for various cases are also tabulated in table 3. For the PISB cases, the values of St_θ are found to be comparable with the literature (Pauley 1994; Watmuff 1999; Rodríguez, Gennaro & Souza 2021). The peak frequencies for the PISB cases are found to decrease at an enhanced level of FST, as clearly seen in figure 9(*g*, *h*). This is attributed to the interaction of the boundary layer streaks with the fore part of the separation bubble, as discussed in § 4.4. This interaction can reduce the distance between the wall and the bubble outline, leading to a reduction in frequency.

Considering the presence/absence of such wall-vortex interaction, a criterion based on integral flow parameters has been proposed to determine whether the shedding frequency will remain the same with and without an enhanced level of FST. The location of a vortex core from the wall can be approximated as δ^*, as discussed earlier. Similarly, on an average, the maximum wall-normal extension of a vortex may be approximated as
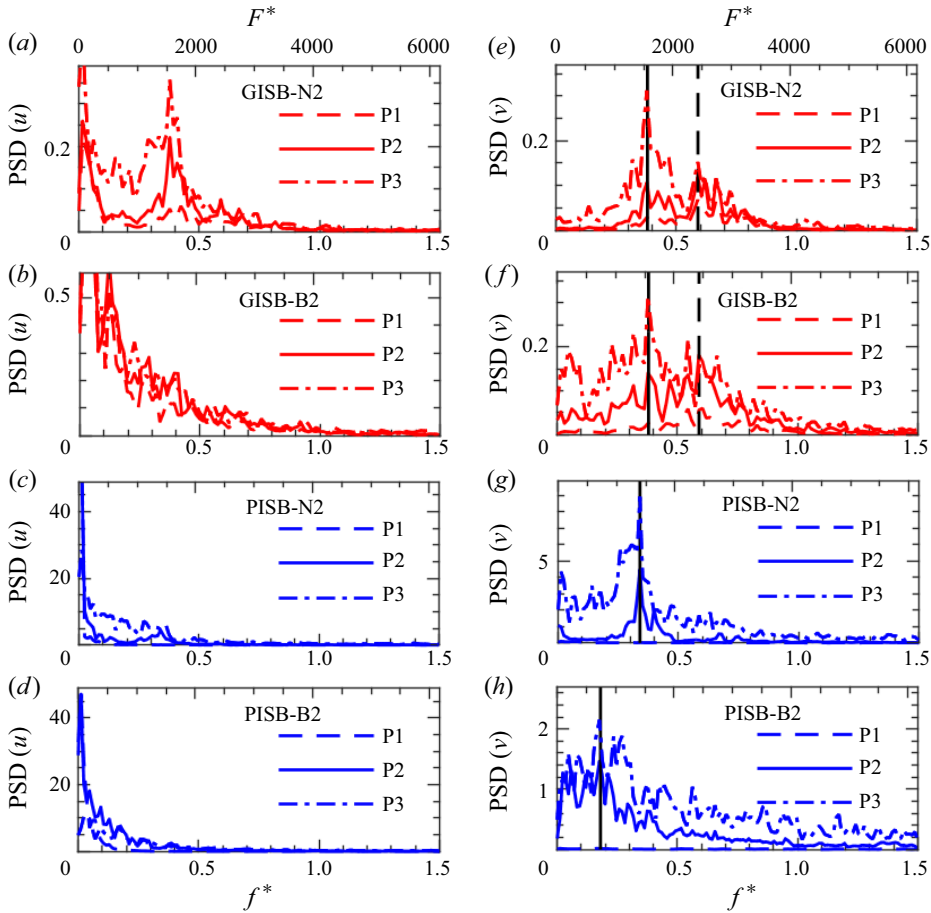
957 A19-20

Figure 9. Power spectral density (PSD) of the fluctuating u and v velocity components at three different locations (P1, P2, P3), as shown by solid white symbols in the first panels of figure 8(*a–d*). (*a–d*) Estimated PSD of u velocity component using Welch's method. (*e–h*) Estimated PSD of v velocity component using Welch's method.

Cases	GISB-N2	GISB-B2	PISB-N2	PISB-B2
$f^*(fh/U_r)$	0.38	0.38	0.34	0.18
$St_\theta(f\theta_s/U_{e,s})$	0.024	0.023	0.012	0.008

Table 3. Measured dominant frequencies for various cases.

the boundary layer thickness, δ, which is defined as the wall-normal height where the local velocity equals U_e. Hence, the distance between the core of a vortex and its top edge can be considered as $(\delta - \delta^*)$. A symmetrical line with respect to the δ^* line can be considered as the bottom edge of the vortex. Therefore, the distance between such a symmetry line and the wall is $\delta^* - (\delta - \delta^*)$, and a vortex well above the wall is expected to be confined within the lines between δ and $\delta^* - (\delta - \delta^*)$. Three white lines representing δ, $\delta - \delta^*$ and $\delta^* - (\delta - \delta^*)$, based on the above discussions, are shown in the last panels
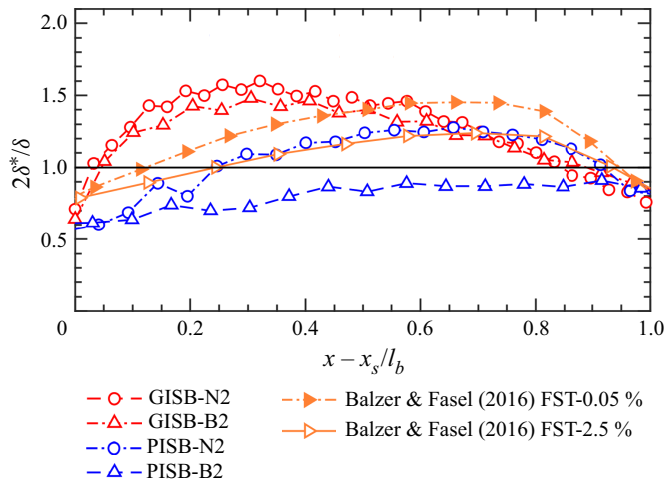
Figure 10. Variation of $2\delta^*/\delta$ along the length of a separation bubble for various cases.

of figure 8(*a–d*), respectively. The core of a vortex, its top and bottom edges are found to be confined well within the lines of δ and $\delta^* - (\delta - \delta^*)$ for the GISB-N2, GISB-B2 and PISB-N2 cases. Hence, when the line $\delta^* - (\delta - \delta^*)$ touches the wall, there is a possibility of a wall-vortex interaction. That is, $\delta^* - (\delta - \delta^*) \leq 0$ or $2\delta^*/\delta \leq 1$ leads to a condition for a wall interaction. It should be noted that the $\delta^* - (\delta - \delta^*)$ line is not shown for the PISB-B2 case because this value is less than zero. However, figure 10 shows that the value of $2\delta^*/\delta$ near the maximum height of the bubble is greater than 1 for the GISB-N2, GISB-B2 and PISB-N2 cases, but it is less than 1 for the PISB-B2 case, indicating the presence of the wall-vortex interaction for this case. The numerical data of Balzer & Fasel (2016) show that the value of $2\delta^*/\delta$ is greater than 1 (see figure 10). This indicates the absence of the wall-vortex interaction, which led to a constant shedding frequency even with an enhanced level of FST in their case. In fact, for further confirmation of the above observation, the TR-PIV measurements were carried out for a different adverse pressure gradient set-up with the same flow condition (not reported here for brevity). Using similar analyses of the TR-PIV data, the present observation was found to be consistent with the new pressure gradient set-up as well.

To ensure the fact that the dominant frequencies in table 3 are associated with the shedding vortices, the POD analysis of the fluctuating v velocity component (v-POD) has been carried out for both the GISB and PISB cases. The v-POD analysis has been performed in the spatial region represented by a rectangle for the GISB cases, as the vortex shedding is found to be active in this zone (see figure 8*a,b*). However, for the PISB cases, the v-POD analysis has been carried out over the entire spatial regions shown in figure 8(*c,d*).

Figure 11 shows the POD analysis of the TR-PIV data for various cases. The relative energy obtained from the v-POD analysis is shown in figure 11(*a–d*) for different cases. In all these cases, the energy of the first two modes is found to be nearly the same. This indicates that the first two modes are coupled, similar to the observation of Lengani *et al.* (2014). It is important to note that the first two modes are also found to be coupled in the PISB-B2 case, even though the wall influence is present, as discussed above. The first and second v-POD modes, as shown in figure 11(*e–h*), for various cases, reveal the same mode shapes with just a spatial shift. A similar shift in time can also be noticed for the
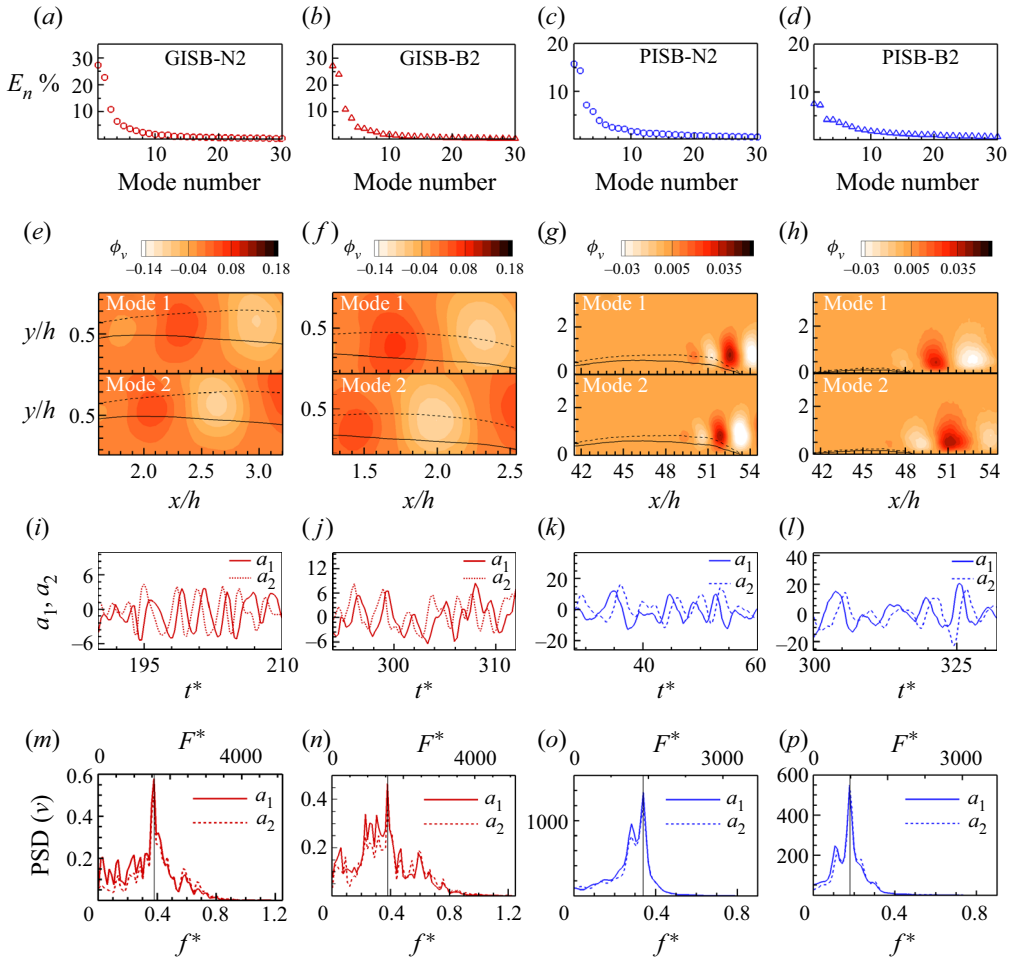
957 A19-22

Figure 11. The POD analysis of the fluctuating v velocity for the data shown in figure 8(a–d). The POD analysis for the GISB cases was carried out in the selected rectangular zones, as shown in the first panels of figure 8(a) and figure 8(b). Figures in (a,e,i,m), (b,f,j,n), (c,g,k,o) and (d,h,l,p) correspond to GISB-N2, GISB-B2, PISB-N2 and PISB-B2 cases, respectively. (a–d) Relative energy of the POD modes for various cases. (e–h) The first and second POD modes. Symbols: ——, $U = 0$ line; - - -, mean dividing streamline. (i–l) Time coefficients of the first and second POD modes. (m–p) The PSD of the time coefficients of the first and second POD modes for different cases.

corresponding time coefficients, a_1 and a_2, as shown in figure 11(i–l). A space–time shift of the POD modes with a nearly equal energy level indicates the presence of a travelling disturbance/wave, and the lack of exact symmetry in the space–time data is attributed to the fact that the associated convecting disturbance is a modulated travelling wave (e.g. Hasan & Sanghi 2007; Mandal *et al.* 2010). The spectra of a_1 and a_2, obtained using the Welch method, reveal nearly the same peak frequency, as shown in figure 11(m–p), for all the four cases. These peak frequency values estimated from the POD analysis for each case are also found to be consistent with the spectral analysis of the actual v velocity signal in the vortex shedding region (see figure 9). Therefore, the first two dominant POD modes represent the vortex shedding around the maximum height of the bubble, revealing the fact that the vortex shedding mode due to the spatially evolving disturbances dominates the
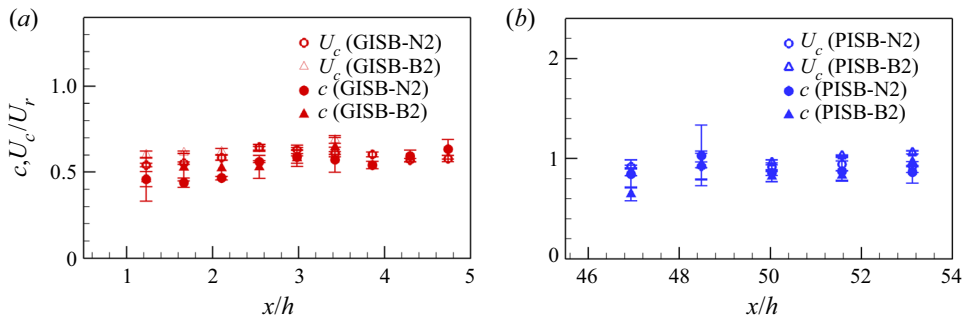
Figure 12. Streamwise variation of the convection and the phase velocity. Results are shown for the (*a*) GISB cases and (*b*) PISB cases.

Cases	Wavelength	Wavenumber
GISB-N2	1.16	5.42
GIBS-B2	1.08	5.82
PISB-N2	2.94	2.14
PISB-B2	4.64	1.35

Table 4. Normalized wavelength and wavenumber estimated from the spatial POD modes for different cases.

separated flow dynamics. Since the vortex shedding frequency decreases for the PISB-B2 case, it is interesting to investigate how the convection/phase velocity and wavelength of the shed vortices contribute to this change.

To find the convection velocity of the vortex shedding, the v fluctuating velocity signal is extracted at $y = \delta^*$ for three different streamwise locations (e.g. at Δx, $2\Delta x$, $3\Delta x$, with an appropriate value of Δx) in the vortex shedding region. Following (e.g. Boutilier & Yarusevych 2012), the cross-correlation analysis of the extracted time-series signals is then carried out to estimate the time taken by the extracted signals to travel from one location to another location. A similar analysis has also been carried out for the filtered velocity field to find out the phase velocity associated with the peak frequencies in figure 11(*m–p*). It should be noted that the filtered velocity field was obtained based on a 1 Hz band pass filter around the peak frequency. However, the convection velocity and the phase velocity, thus obtained, are found to be nearly constant even at an enhanced level of FST, as shown in figures 12(*a*) and 12(*b*), for the GISB and PISB cases, respectively. It is interesting to note that the convection velocity and the phase velocity remain the same either for the GISB or the PISB cases with and without an enhanced level of FST, even though the wall influence is present for the PISB-B2 case.

Similarly, using the v-POD analysis in the shedding region, we estimated the wavelength of the shed vortices. As the positive and negative regions of the spatial v-POD modes (for example, see figure 11*e–h*) are associated with a shedding structure, the distance between peak-to-peak/crest-to-crest of the spatial data extracted along the streamwise direction (at approximately $y = \delta^*$) provides the wavelength of the shed vortices (e.g. Lengani *et al.* 2014). The normalized values of the wavelength and the wavenumber are given in table 4. Even at an enhanced level of FST, the wavelength of the shed vortices is found to be nearly the same for the GISB cases, whereas it is found to change for the PISB cases.

957 A19-24
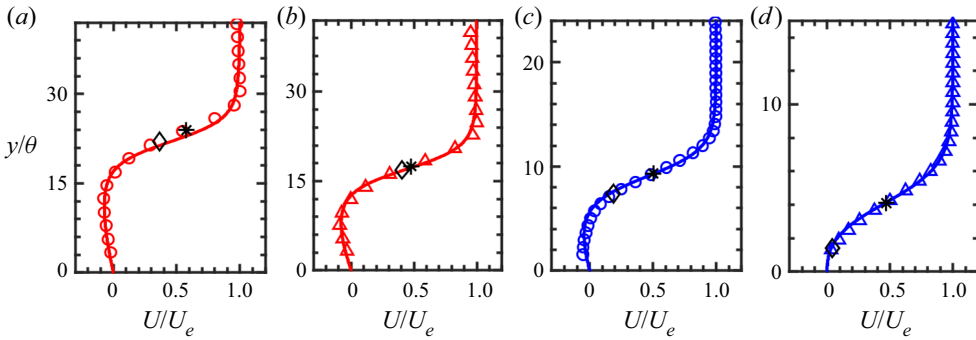
Figure 13. Dovgal's curve fit to the measured velocity profiles at different locations. Symbols: ○, measured data; —, Dovgal's curve fit; *, location of the inflection point (y_{in}); ◇, location of the mean dividing streamline (y_d). (*a*) Velocity profile for the GISB-N2 case at $x/h = 1.26$ with curve-fit constants, $a = 0.262$, $b = -0.075$, $d = 22$. (*b*) Velocity profile for the GISB-B2 case at $x/h = 0.94$ with curve-fit constants, $a = 0.3002$, $b = -0.09$, $d = 13.7$. (*c*) Velocity profile for the PISB-N2 case at $x/h = 50.03$ with curve-fit constants, $a = 0.3718$, $b = -0.08$, $d = 8.353$. (*d*) Velocity profile for the PISB-B2 case at $x/h = 46.93$ with curve-fit constants, $a = 0.427$, $b = -0.038$, $d = 4.096$.

4.3. *Linear stability analysis*

The analyses in the previous section show that the vortex shedding at an enhanced level of FST is not bypassed for both the GISB and PISB cases. It is then legitimate to ask whether a LSA, even for the case of an enhanced level of FST, can describe the disturbance characteristics. Various curve fits are often utilized to fit the measured mean velocity data in a separation bubble for the local stability analysis based on the parallel flow assumption (e.g. Boutilier & Yarusevych 2012; Balzer & Fasel 2016). Even though the separated flow is not strictly parallel, the results of the LSA based on the parallel flow assumption closely represent the experimental observations (e.g. Diwan & Ramesh 2009; Boutilier & Yarusevych 2012; Diwan & Ramesh 2012). However, following the works of Boutilier & Yarusevych (2010, 2012), we use the fit proposed by Dovgal *et al.* (1994), that is,

$$U(y_1) = [\tanh(a(y_1 - d)) + \tanh(ad)]/[1 + \tanh(ad)] + b\sqrt{3}\exp\left[-1.5\frac{y_1^2}{d^2} + 0.5\right].$$
(4.1)

Here, the constant b is used to control the backflow in the velocity profiles, the constant, d, is the normalized distance of the inflection point from the wall, and the variable, y_1, is the normalized distance from the wall. The momentum thickness, θ, and the shear layer edge velocity, U_e, are used as the length and the velocity scales for normalization, respectively. The constant, a, has to be fixed based on the fact that the equation, $\int_0^\infty U(y_1)[1 - U(y_1)]\,dy_1 = 1$, is satisfied.

Figure 13 shows the experimentally measured and the corresponding fitted velocity profiles for different cases. These velocity profiles are chosen at the streamwise locations where $v_{rms,max}$ begin to grow exponentially (see figure 7*e,f*). The curve-fitted velocity profiles closely follow the experimental data. Wall-normal locations of the mean dividing streamline (y_d) and the point of inflection (y_{in}) are also shown in figure 13. One may notice that the point of inflection lies above the mean dividing streamline for all the velocity profiles. This observation appears to be consistent for some other streamwise locations as well, as the ratio of y_{in} to y_d is found to be greater than 1 at those locations, as shown in
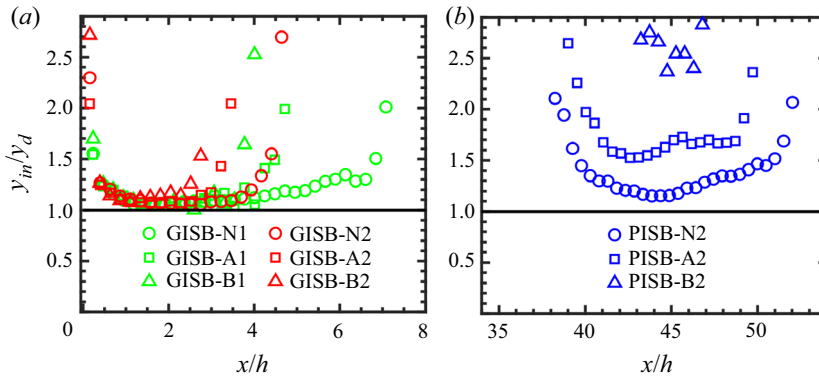
Figure 14. A ratio of y_{in}/y_d along the streamwsie direction. Results are shown for the (*a*) GISB cases and (*b*) PISB cases.

figure 14. Based on the stability analyses of some analytical base flow profiles $U(y)$ in a separation bubble, Avanci, Rodríguez & Alves (2019) found $y_{in} \leq 0.9y_d$ for the absolute instability of the base flow profiles. Although the present numerical values of y_{in} for the PISB cases are clearly greater than $0.9y_d$, the values of y_{in} for the GISB cases at some streamwise locations are found to be just marginally higher than the proposed critical value. Therefore, it is difficult to rule out the presence of absolute instability at least for the GISB cases, as the non-parallel effect is also significant for the GISB cases (see figure 3). The different dynamics and the characteristics between the GISB and PISB cases may also be related to the fact that a GISB is more prone to be absolutely unstable as compared with a PISB. However, further studies are essential for a strong conclusive outcome in this regard.

To determine the spatial linear stability characteristics of the velocity profiles, as shown in figure 13, the OSE and Rayleigh equations, as detailed in § 3.2, are solved considering parallel flow approximation. Figure 15 shows the growth rates $(-\alpha_i h)$ variation with $f^*(= fh/U_r)$ for the above velocity profiles. In this figure the normalized circular frequency, $\omega^*(= \frac{1}{4}\delta_w(2\pi f/U_m))$, and the spectra obtained from the v-POD analysis are also superposed for comparison purposes. Here, δ_w and U_m denote the vorticity thickness and the average of the minimum and maximum velocities in the separated shear layer, respectively (see Diwan and Ramesh 2009, for details). The peak frequencies obtained from the viscous and the inviscid stability analyses for the respective cases are found to be the same, with nearly comparable maximum growth rates for the viscous (OSE) and inviscid (Rayleigh) calculations. Also, the growth rates are nearly the same for both the GISB cases with and without an enhanced level of FST, whereas a reduction in growth rates can be seen for the PISB case with an enhanced level of FST, as compared with the case without an enhanced level of FST. This is attributed to the presence of streamwise velocity streaks, as discussed below in § 4.4; these streaks can modify the distance between the inflection point and the wall, eventually leading to a reduction of the growth rate with an increase of FST level. Most importantly, we find that the experimental peak frequencies closely follow the most unstable frequencies obtained from the LSA, even for an enhanced level of FST. Moreover, figure 15 reveals that, with and without an enhanced level of FST at the same free-stream velocity, the most unstable frequency/shedding frequency is nearly constant for the GISB cases, whereas it changes for the PISB cases.

The existence of periodic vortex shedding from the separated shear layer is often attributed to the KH instability mechanism (e.g. Watmuff 1999; Spalart & Strelets 2000;
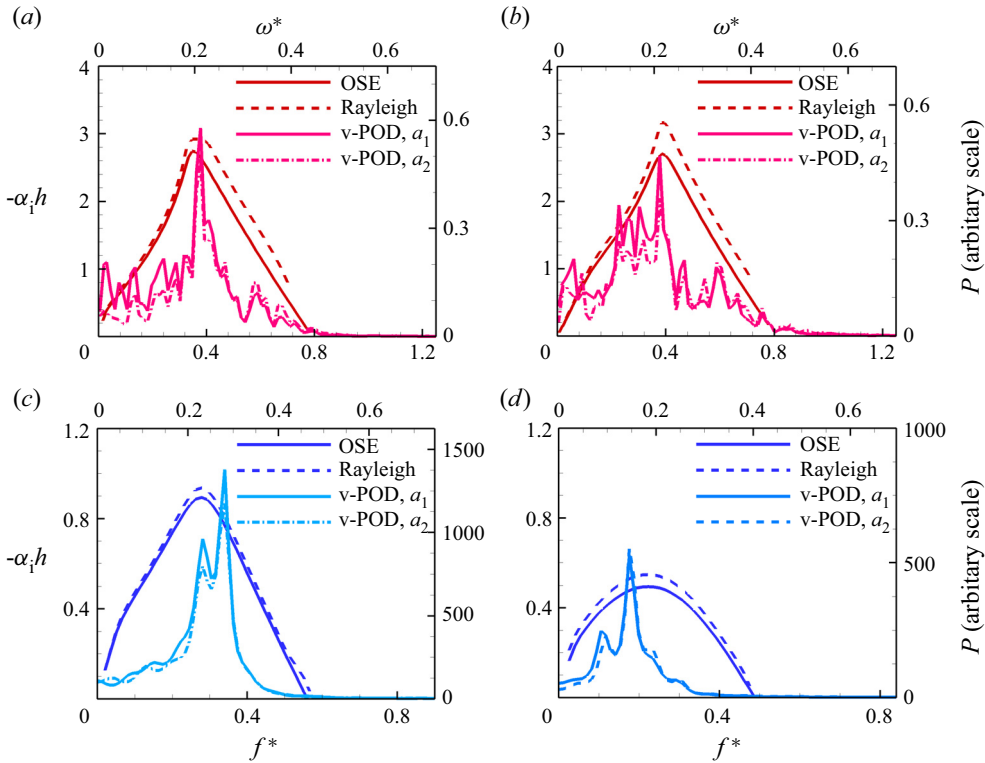
957 A19-26

Figure 15. Calculated spatial growth rates obtained from the LSA for the corresponding velocity profiles shown in figure 13. The PSD of POD time coefficients for the first and second POD modes, as shown in figure 11(*m–p*), are reproduced here for comparison purpose. Results are shown for the (*a*) GISB-N2 case, (*b*) GISB-B2 case, (*c*) PISB-N2 case, (*d*) PISB-B2 case.

Simoni *et al.* 2012*a*). A criterion based on the normalized circular frequency, ω^*, is often used to determine the presence of such a mechanism (e.g. Watmuff 1999; Simoni *et al.* 2012*a*,*b*). The criterion is actually adopted from the inviscid stability analysis of a mixing layer velocity profile by Monkewitz & Huerre (1982) who found $\omega^* = [0.21 \quad 0.22]$ for a wide range of velocity ratios. However, we find the value of $\omega^* \approx 0.21$ for the GISB-N2, GISB-B2 and PISB-N2 cases, whereas it is approximately ≈ 0.18 for the PISB-B2 case. Based on the ω^* criterion, the inviscid instability mechanism is bypassed for the PSIB-B2 case, even though the present linear stability analyses can closely describe the shedding frequency for this case as well. Therefore, it can be inferred that the ω^* criterion is not valid for the PISB-B2 case. Furthermore, the wavenumber spectra for the unstable modes are also found to compare well with the experimentally estimated wavenumbers even at an enhanced level of FST, as shown in figure 16; here, the wavenumbers were estimated using the frequency and the phase velocity, as discussed in § 4.2. Similarly, the eigenmodes closely match with their experimental counterparts within the unstable band of the linear stability frequency, as shown in figures 17 and 18, for the GISB and the PISB cases, respectively. In fact, a better match can be seen at approximately the shedding frequency for all the cases. It should be emphasised that even though the shedding frequency changes at an enhanced level of FST for the PISB-B2 case, the LST mode shape still matches with its experimental counterpart. For all the cases, these figures also show that the eigenmodes obtained from the OSE and the Rayleigh equations are found to be the same except very
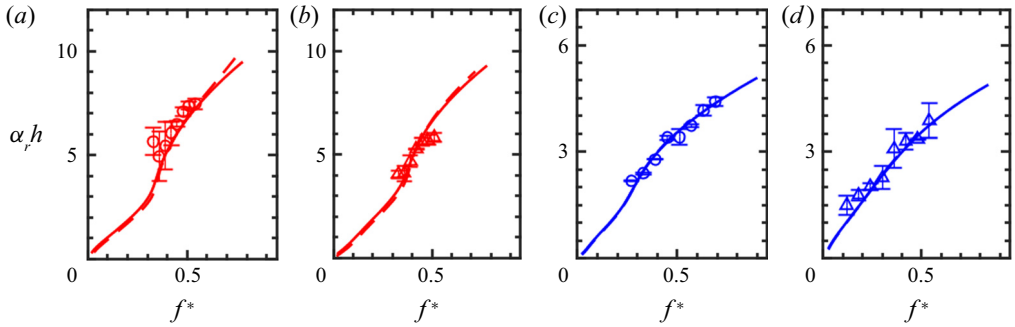
Figure 16. Wavenumber spectrum obtained from the LSA and the estimated wavenumber obtained from the experimental data at x/h = 1.23, 1.89, 50.03 and 46.93 for the (*a*) GISB-N2 case, (*b*) GISB-B2 case, (*c*) PISB-N2 case and (*d*) PISB-B2 case, respectively. Description of lines: solid line, viscous (OSE) solution; dashed line, inviscid (Rayleigh) solution. Symbols with error bars represent experimental data.
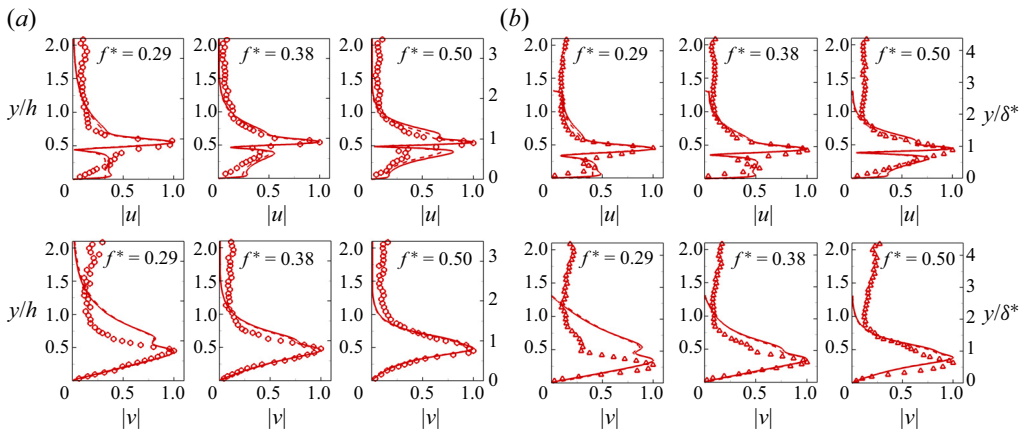

Figure 17. Comparison of the eigenmodes with their experimental counterparts for the GISB cases; here, $| u | (= \frac{|\hat{u}|}{|\hat{u}|_{max}})$ and $| v | (= \frac{|\hat{v}|}{|\hat{v}|_{max}})$ are the magnitudes of u and v eigenfunctions, respectively. Experimental eigenmodes are obtained from the r.m.s. values of the filtered velocities. Results are shown for the (*a*) GISB-N2 and (*b*) GISB-B2 cases. Description of lines: −, red, viscous (OSE) solution; −−, red, inviscid (Rayleigh) solution. Symbols: ○, red and △, red, experimental data.

close to the wall. The occurrences of the peak of the mode shapes at $y \approx \delta^*$ also lead to the fact that the disturbances get amplified due to the inflectional instability mechanism, as the point of inflection in the velocity profile is found to be at $y_{in} = \delta^*$ (Marxen, Lang & Rist 2012). Being guided by the work of Villermaux (1998), and using the inviscid LSA of a piecewise linear velocity profile in the presence of a wall, Diwan & Ramesh (2009) arrived at

$$\frac{f(y_{in}^2 + \delta_w^2)}{\nu} \sim \frac{U_{in}y_{in}}{\nu}\sqrt{\frac{y_{in}}{\delta_w}} \left(= \bar{R}\sqrt{\frac{y_{in}}{\delta_w}}\right) \tag{4.2}$$

for the most amplified linear stability frequency. The present data, with and without an enhanced level of FST, compare very well with their scaling relation, as shown in figure 19(*a*). However, as the present study reveals that $U_{in}/U_e = 0.5$ (figure 5), and
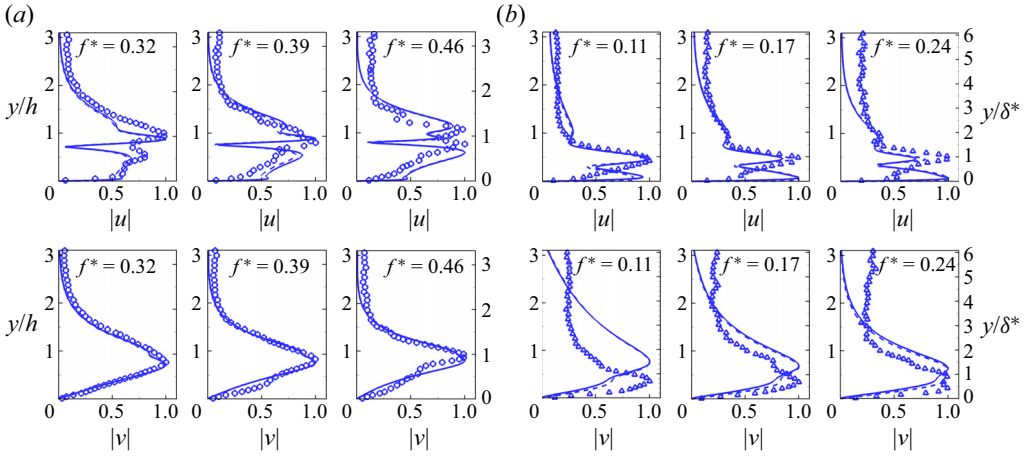
957 A19-28

Figure 18. Comparison of the eigenmodes with their experimental counterparts for the PISB cases; here, $|u| \left(= \frac{|\hat{u}|}{|\hat{u}|_{max}}\right)$ and $|v| \left(= \frac{|\hat{v}|}{|\hat{v}|_{max}}\right)$ are the magnitudes of u and v eigenfunctions, respectively. Experimental eigenmodes are obtained from the r.m.s. values of the filtered velocities. Results are shown for the (*a*) PISB-N2 and (*b*) PISB-B2 cases. Description of lines: −, blue, viscous (OSE) solution; −−, blue, inviscid (Rayleigh) solution. Symbols: ○, blue and △, blue, experimental data.
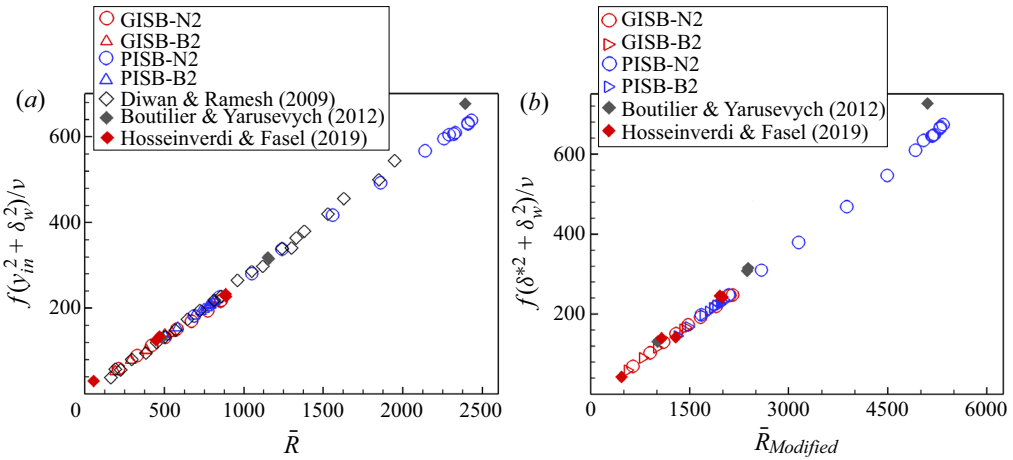

Figure 19. (*a*) Comparison of the most amplified frequency with the scaling relation of Diwan & Ramesh (2009). (*b*) Comparison of the most amplified frequency with the modified scaling relation.

$y_{in} \approx \delta^*$ (figures 3 and 4), the above scaling relation can be recast as

$$\frac{f(\delta^{*2} + \delta_w^2)}{\nu} \sim \frac{U_e \delta^*}{\nu} \sqrt{\frac{\delta^*}{\delta_w}} \left(= \bar{R}_m \sqrt{\frac{\delta^*}{\delta_w}} \right). \tag{4.3}$$

This modified relation is also found to be universal, as it holds good not only for the present data but also for the available data in the literature, as shown in figure 19(*b*). In fact, with a proportionality constant, one can easily estimate the most unstable frequency for a given velocity profile from the modified scaling relation, as it is easier to find the values of U_e and δ^* as compared with the values of U_{in} and y_{in} from an experimental velocity profile.

The growth rates, the wavenumber spectra and the eigenmodes (figures 15–19), as obtained from the solutions of the Rayleigh and the OSEs, are closely comparable.

957 A19-29

This is expected as the velocity profiles in separated flows are usually inflectional in nature (figure 5). The experimental data also compare well with these results. These observations imply that, for both the GISB and PISB cases, the inviscid inflectional instability mechanism dominates the disturbance growth in a separated shear layer even at an enhanced level of FST. Therefore, one needs to be careful enough to conclude that the linear stages of transition are bypassed just based on the fact that ω^* is less than 0.21, as found for the PISB-B2 case (see figure 15), or the shedding frequency peak is not detectable in the spectra of the u velocity signal, or the peak frequency reduces at an enhanced level of FST.

4.4. *Unsteady flow characteristics in the wall-parallel (x–z) plane*

To investigate the nature of the spanwise flow inside a separation bubble, the conventional PIV measurements have been carried out in the spanwise plane located at $y/h = 0.167$ ($y = 2$ mm) for both the GISB and PISB cases. One may note that this wall-normal height corresponds to $y/\delta_{max}^* = 0.2, 0.3, 0.15, 0.3$ for the GISB-N2, GISB-B2, PISB-N2 and PISB-B2 cases, respectively. Here, δ_{max}^* represent the maximum displacement thickness value estimated from the wall-normal plane measurement. Figure 20(*a–d*) shows the typical four instantaneous PIV realizations in the spanwise plane for four different cases. Patterns of the instantaneous velocity contours and the fluctuating velocity vectors are not indicative of unsteady streaky structures for both the GISB cases. Instead, small Λ-like patterns in the instantaneous velocity contours are clearly visible for both the cases (i.e. for the cases with and without a turbulent generating grid in the test section). Our measurements at the lower Reynolds number indicate that these Λ-like patterns perhaps originate due to the distortion of the spanwise roller structures (not shown here for brevity). The streaky structures in a transitional boundary layer at an enhanced level of FST usually show elongated high- and low-velocity regions often accompanied by organized positive and negative u fluctuations in the streamwise directions (e.g. Jacobs & Durbin 2001; Mandal *et al.* 2010; Balamurugan & Mandal 2017). Since figure 20(*c*) does not show any such feature, one can be assured that the streaky structures are absent for the PISB-N2 case. On the other hand, one can clearly see the signature of streaky structures in figure 20(*d*) for the PISB-B2 case with an increasing level of FST, as the velocity contours reveal elongated high- and low-velocity regions dominated by organized positive and negative u fluctuations (as the w component is negligible), respectively. This indicates the clear existence of the K mode for the PISB-B2 case with an enhanced level of FST, similar to the numerically simulated ones reported by Balzer & Fasel (2016). These instantaneous observations are also statistically verified using the linear stochastic analyses detailed in Appendix A (see figure 25 in Appendix A).

The above results for the PISB at an enhanced level of FST clearly show the high- and low-velocity streaks in a separated boundary layer. However, the role of these streaky structures in the secondary instability process of a roller vortex has not been addressed in the literature, to the best of our knowledge. For such an investigation, the TR-PIV measurements in the spanwise plane at different wall-normal locations are carried out for the PISB cases.

The time sequences of the fluctuating velocity fields at two different wall-normal locations, $y/h = 0.8$ and $y/h = 1.3$ that corresponds to $y/\delta_{max}^* = 0.9, 1.3$, are shown in figures 21(*a*) and 21(*b*), respectively, for the PISB-N2 case. This figure shows some periodical patches of intense velocity fluctuations embedded in the spanwise roller, as identified from the u velocity contours. These patches are often accompanied by some
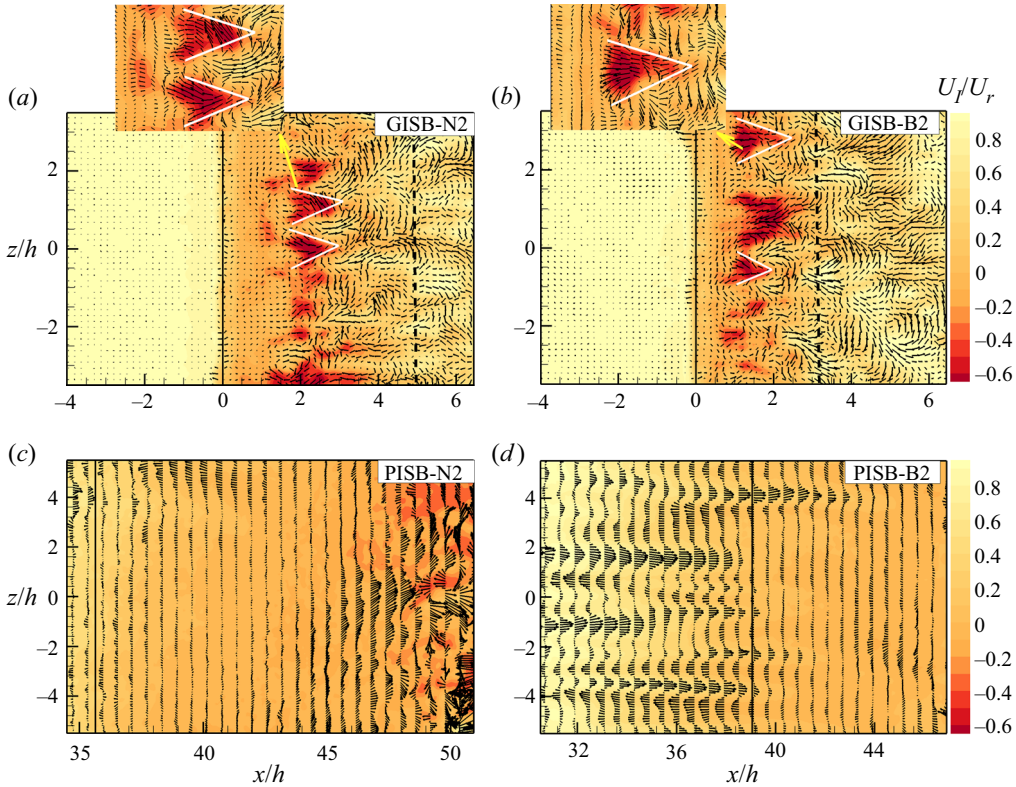
Figure 20. Four typical instantaneous PIV realizations in the spanwise plane for four different cases (*a–d*). Fluctuating velocity vectors are overlaid with the contours of the instantaneous streamwise velocity in the spanwise plane. Black solid and dashed lines show approximate separation and reattachment locations for each case. The zoomed view of the Λ-like structure for the cases of GISB-N2 and GISB-B2 are shown by the subfigures in (*a,b*), respectively.

counter-rotating vortices as identified by the swirling strength contour, which is the imaginary part of the complex eigenvalue of the local velocity gradient tensor (Chong, Perry & Cantwell 1990; Adrian, Christensen & Liu 2000). However, this indicates the secondary instability of the separated shear layer. The spanwise wavelengths (λ_z) of these patches (see figure 21*a*) at $y/h = 0.8$ and $y/h = 1.3$ are found to be $1.9(\pm 0.3)$, and $2(\pm 0.3)$, respectively. Considering the streamwise wavelength (λ_x) from table 4, the ratio, λ_z/λ_x, is found to be 0.64 and 0.68 at $y/h = 0.8$ and 1.3, respectively. These values are within the range (0.41–1) reported in the literature (e.g. Marxen *et al.* 2013; Michelis, Yarusevych & Kotsonis 2018*b*; Michelis, Kotsonis & Yarusevych 2018*a*; Hosseinverdi & Fasel 2019) for the PISBs. Interestingly, the present data compare well with the translative instability value ($\lambda_z/\lambda_x = 0.67$) of a mixing layer (Pierrehumbert & Widnall 1982). This secondary instability is due to the stretching of the spanwise vortex in the streamwise direction. The TR-PIV measurements in the wall-normal plane clearly reveal that the shear layer roll-up is not bypassed even at an enhanced level of FST, and the shedding frequency can also be described by the linear instability analysis. Then an obvious question is: What is the role of a boundary layer streak in a separated shear layer? To elucidate this, time sequences of some TR-PIV realizations at two different wall-normal locations $y/h = 0.4$ and 0.8 that corresponds to $y/\delta^*_{max} = 0.8$ and 1.6, are shown in figures 22(*a*) and
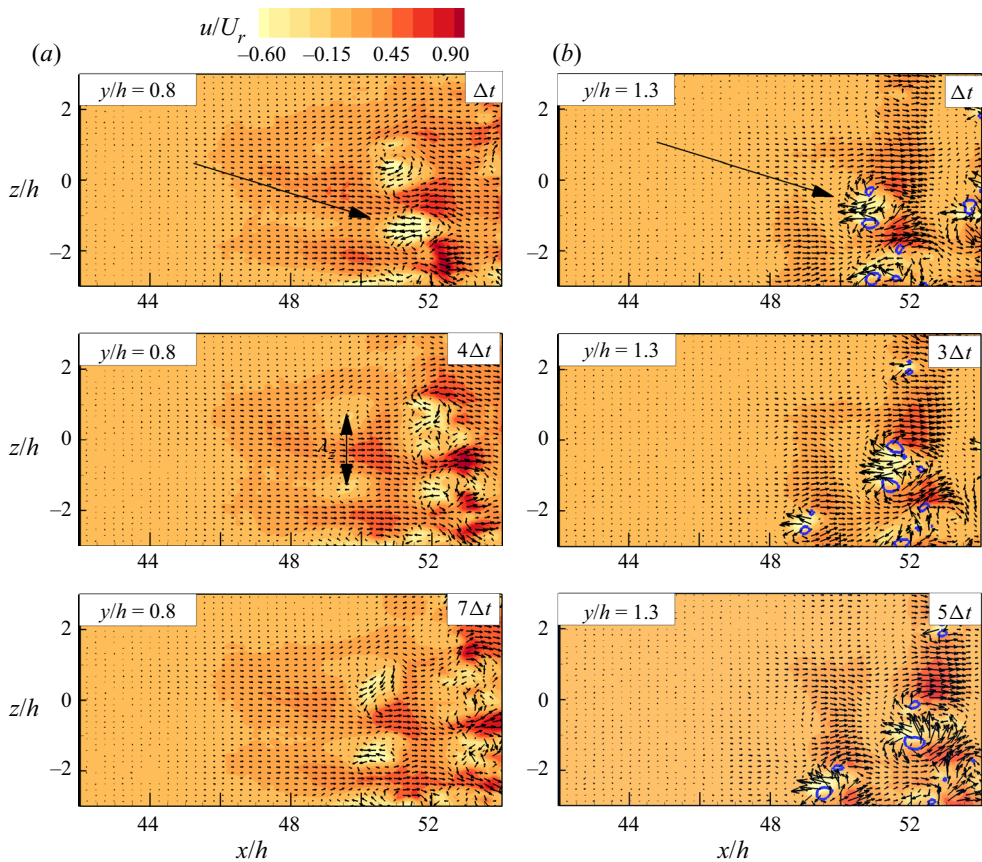
Figure 21. An instability in the spanwise plane for the PISB-N2 case. (*a,b*) Fluctuating velocity components of *u* and *w* are superimposed with the *u* fluctuating velocity contour at $y/h = 0.8$, $y/h = 1.3$, respectively. Swirling strength contour lines (blue coloured) are also shown over the contour of the *u* fluctuating velocity in figure (*b*).

22(*b*), respectively. An oscillating low-speed streak, as indicated by a black arrow, can clearly be seen in figure 22(*a*). From such similar sinuous streak oscillations, Lengani *et al.* (2017) concluded that the streak oscillation leads to the streak breakdown, initiating the transition process in a PISB subjected to an enhanced level of FST. On the other hand, the present oscillating streak is not seen to break down to progressively smaller scales. Interestingly, the measurements at a higher wall-normal location (at $y/h = 0.8$) do not reveal any streaky structure (see figure 22*b*). However, one can clearly see some packets of intense fluctuations, as shown in figure 22(*b*). These small intense fluctuations are accompanied by some counter-rotating vortices, as identified by the swirling strength contours. The spatial distribution of these packets clearly reveals a Λ-like inclined structure in the spanwise plane (marked by a white coloured line), which seems to have originated from the spanwise roller. This suggests that the streaky structures are perhaps responsible for the distortion of the spanwise roller.

To better understand the interaction of a streaky structure with the spanwise roller, another time sequence of the instantaneous velocity fields is shown in figure 23(*a*). A streaky structure around $z/h = 0$ can clearly be seen in this figure until $x/h \approx 52$. The streaky structure is followed by a Λ-like spanwise structure, which is indicated by
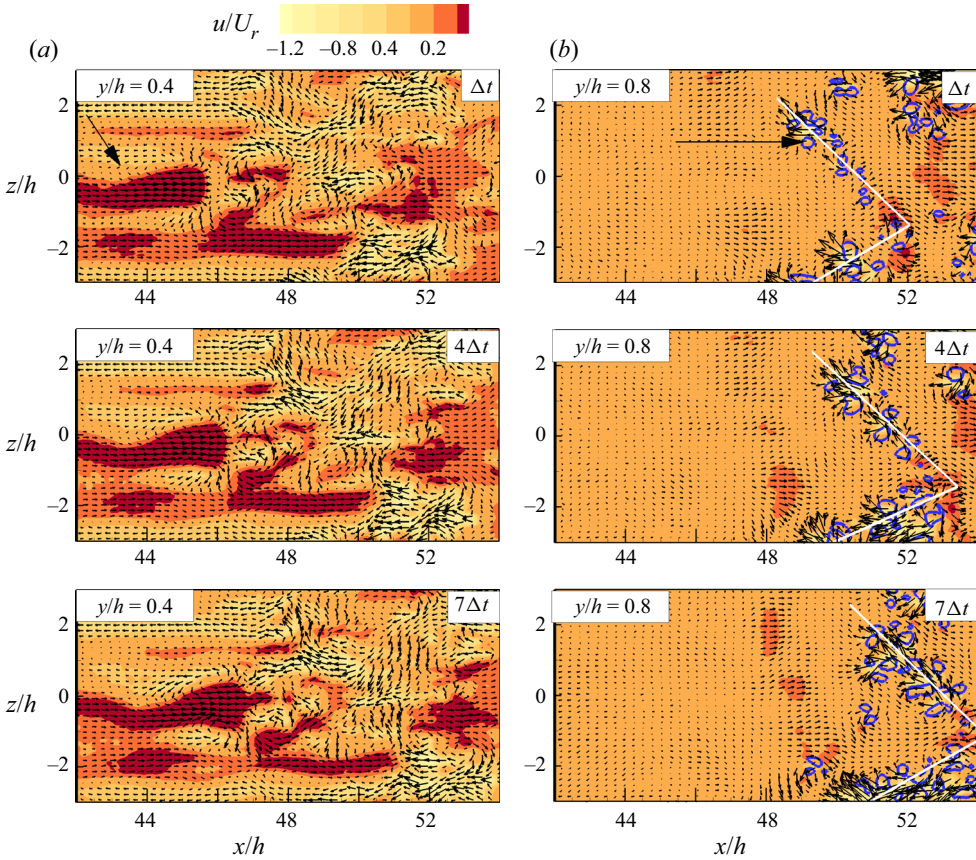
957 A19-32

Figure 22. An instability in the spanwise plane for the PISB-B2 case. (*a,b*) Fluctuating velocity vectors of u and w are superimposed with the contours of u fluctuation at $y/h = 0.4$ and $y/h = 0.8$, respectively. Line contours of the swirling strength (in blue) are also shown over the contour of u fluctuation in (*b*). The arrows in the first panels of (*a,b*) indicate an oscillating streak and the small vortices, respectively.

a black line in figure 23(*a*). To decipher the hidden information in figure 23(*a*), the fluctuating velocity components are filtered at the low-frequency band ($f^* < 0.03$) and band pass filtered at approximately the peak frequency of $f^* = 0.18$. It should be noted that the choice of $f^* < 0.03$ for the low-frequency band corresponds to $2\pi f \nu \times 10^6 / U_e^2 \le 35$, as this value corresponds to low-frequency fluctuations due to the streaky structures (see Westin *et al.* 1994; Balamurugan & Mandal 2017, for details). The filtered velocity fields corresponding to the low and peak frequency bands are shown in figures 23(*b*) and 23(*c*), respectively. Even though the instantaneous flow field shows the streak-shedding structure interaction, this filtering band isolates the streaky structure and the Λ-like structures, as shown in figures (*b*) and (*c*), respectively. For better illustration of the Λ-like structures, white and black coloured lines are drawn over the positive and negative u fluctuating velocity, respectively, as shown in figure 23(*c*). The same lines are also drawn in figure 23(*a*) at the same location. These lines indicate the hidden Λ-like structure in the instantaneous flow field. This suggests that a streaky structure does not take part in the transition process through the streak breakdown process at least for the FST level of 3.3 %. Instead, it takes part in the secondary instability process of a separated shear layer by distorting the spanwise roller, which is also present at an enhanced level of FST.
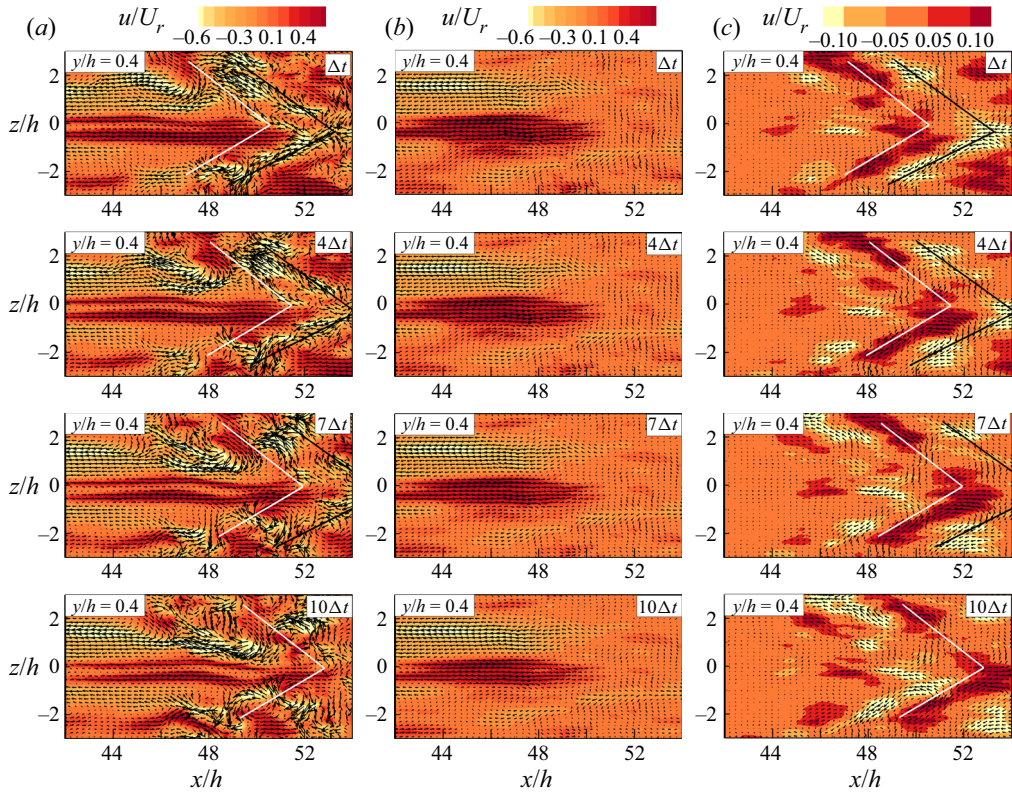
Figure 23. Fluctuating velocity vectors ($u - w$ component) superimposed with a u fluctuating velocity contour for the PISB-B2 case at $y/h = 0.4$. (*a*) Instantaneous measurement. (*b*) Filtered data at $f^* < 0.03$. (*c*) Filtered data at $f^* = 0.18$.

Furthermore, this figure also indicates that the KH instability mechanism is still dominant at an enhanced level of FST.

For further clarification of the role of streaky structures in the formation of a Λ-like structure, we calculated the spectral disturbance kinetic energy (SDKE) for the PISB-B2 case following Hosseinverdi & Fasel (2019). The filtered fluctuating velocity components at the low-frequency band ($f^* < 0.03$) and the band pass filtered components at approximately the peak frequency of $f^* = 0.18$ are used to identify the contribution of the streaks and the KH instability/shedding structure for the transition process, respectively; the filtered fluctuating velocities in the streamwise, wall-normal and spanwise directions are denoted as $u_{filtered}$, $v_{filtered}$, $w_{filtered}$, respectively. However, the SDKE has been calculated for both the x–y and x–z planes, and the spanwise plane has been considered at $y/h = 0.4$, as the clear interaction of the streaks with the spanwise rollers can be seen in this plane (figure 23). For the x–y plane, the disturbance kinetic energy, E_{xy}, has been calculated as

$$E_{xy} = \frac{1}{2U_r^2\delta} \int_0^\delta [u_{filtered}^2(y) + v_{filtered}^2(y)] \, \mathrm{d}y, \tag{4.4}$$

where U_r and δ are the reference velocity and boundary layer thickness, respectively. Similarly, for the x–z plane at $y/h = 0.4$, the disturbance kinetic energy, E_{xz}, has been
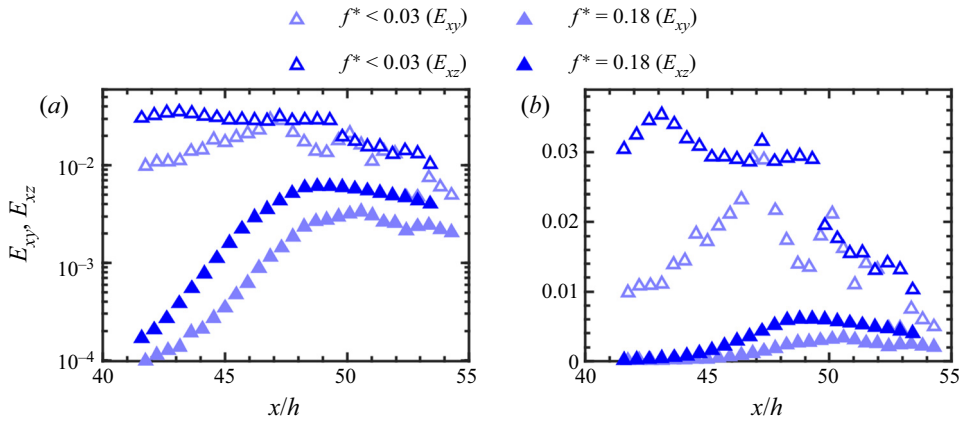
957 A19-34

Figure 24. Comparison of integrated spectral disturbance kinetic energy growth for the PISB-B2 case. (*a*) Log scale. (*b*) Linear scale.

calculated as

$$E_{xz} = \frac{1}{2U_r^2(z_1 - z_0)} \int_{z_0}^{z_1} [u^2_{filtered}(z) + w^2_{filtered}(z)]\,dz, \qquad (4.5)$$

where z_0 and z_1 are the end points in the *x–z* plane.

Figure 24 shows the variations of E_{xy} and E_{xz} in the streamwise direction. To investigate whether the energy growth is exponential or transient, the variations have been plotted both in semi-log and linear scales, as shown in figures 24(*a*) and 24(*b*), respectively. Note that the unfilled symbols correspond to the low-frequency disturbance, which is associated with the streaky structures, and the filled symbols correspond to the peak frequency, which is associated with the KH instability/shedding structure. Figure 24(*a*) shows that the energy associated with the filtered data at approximately the shedding/peak frequency of $f^* = 0.18$ grows exponentially in the streamwise direction. For transient energy growth, it is expected to grow linearly, as commonly seen for the streaky structures in attached boundary layers at an enhanced level of FST (e.g. Matsubara & Alfredsson 2001; Balamurugan & Mandal 2017). But figure 24(*b*) does not show such linear growth. In fact, a small exponential growth can be observed in the *x–y* plane data even for the low-frequency boundary layer streaks (see figure 24*a*). A similar variation is also observed in the numerical study of Hosseinverdi & Fasel (2019). However, figure 24 shows that the energy associated with the low-frequency streaky structures is higher than the vortex shedding mode. Nevertheless, the exponential growth associated with vortex shedding is not suppressed or bypassed due to the presence of streaky structures. This indicates that the streaky structures do not play a significant role in bypassing the vortex shedding, rather it distorts the vortex shedding structure of the spanwise roller.

The above transition scenario cannot be generalized as it may depend on the disturbance amplitude at the point of separation. However, the present study at least ensures that the vortex shedding/the KH mechanism will not be bypassed if $u_{rms,max}/U_e \leq 0.1$ at the point of separation as the value of $u_{rms,max}/U_e$ is found to be 0.1 at the point of separation for the PISB-B2 case.

5. Summary and concluding remarks

An experimental study using both the conventional and the TR-PIV techniques was carried out in a GISB and a PISB for a comparative assessment of these bubbles with and without an enhanced level of FST. The GISB was generated using a blunt leading edge of a flat plate, whereas a PISB was generated over a flat plate by imposing an adverse pressure gradient in the flow using a contoured wall. Two different passive turbulent generating grids were used to generate nearly isotropic FST. For a comparative study on the GISB and the PISB, the measurements were carried out at a constant reference velocity in the free stream.

Mean flow data reveal that the length and height of a separation bubble decrease with increasing FST and Reynolds number (see figures 3 and 4), consistent with the literature. However, we find that the bubble outlines, identified either using $U = 0$ or using $\int_0^{y_d} U \, dy = 0$, collapse at the initial stage for all the GISB cases, whereas the corresponding outlines for the PISB cases with and without an enhanced level of FST do not show such characteristics (see figure 6a–d). This is mainly due to the presence of the streamwise elongated streaks for the PISB cases at an enhanced level of FST. Interestingly, normalizing the mean dividing streamline and the length of a separation bubble with its maximum height and maximum length, the bubble outlines based on the mean dividing streamline are found to collapse separately for the GISB and the PISB cases with and without an enhanced level of FST (see figures 6f and 6h, respectively). This observation has also been substantiated by the available data in the literature.

The TR-PIV measurements in the wall-normal plane show that the vortex shedding from the separated shear layer is not bypassed at an enhanced level of FST for both the GISB and PISB cases. In the case of GISB, we find that the vortex shedding frequency does not change with FST at constant Re_h, whereas the vortex shedding frequency decreases with FST for the PISB cases. The reduction in frequency is found to be mainly due to an increase in the wavelength of the shed vortices, as the phase velocity of the dominant disturbance associated with the vortex shedding remains constant. The most amplified frequency, the corresponding eigenfunction and the wavenumber obtained from the LSA of the mean velocity profiles are found to compare well with their experimental counterparts. Moreover, we proposed a modified scaling relation for the most amplified frequency using U_e and δ^*, which is found to be universal. Linear stability analysis reveals that the linear instability mechanism is not bypassed even at an enhanced level of FST for both GISB and PISB cases. In fact, it confirms that the inviscid/KH instability is present even though the vortex shedding frequency reduces with FST for the PISB case. Hence, the absence of constant vortex shedding frequency does not ensure whether the inviscid/KH instability is present or not. However, we propose a criterion based on the integral flow parameter when the vortex shedding frequency will remain constant and when it will not, as is also verified using the published data in the literature (Balzer & Fasel 2016).

The PIV measurements in the spanwise plane clearly reveal that the laminar streaks are not present for a GISB even at an enhanced level of FST, whereas the laminar streaks are clearly seen for the PISB at an enhanced level of FST. Instead of streaky structures in the spanwise plane for the GISB cases, small Λ-like structures are seen. Furthermore, the TR-PIV measurements in the spanwise plane for the PISB case without an enhanced level of FST reveal the existence of a 2-D roller structure due to the primary instability, and the secondary instability of the separated shear layer resembles the translative-type instability that occurs in a planar mixing layer. Whereas, at an enhanced level of FST, the boundary layer streaks near the point of separation are found to interact with the separated shear layer. This interaction is seen to exist even near the maximum height of the bubble.

The present experimental study clearly reveals that the boundary layer streaks do not bypass or suppress the primary instability/KH instability, rather distort the 2-D roller structure, which is associated with the primary instability, into a Λ-like structure. Therefore, the Λ-like structures, as seen here, are not due to the streak oscillation or its breakdown due to the streak secondary instability. As per the present data, this transition scenario is valid until the $u_{rms,max}/U_e$ value reaches 0.1 at the point of separation for the PISB. However, this may not be a general transition mechanism at an enhanced level of FST, as one needs to investigate what happens if the $u_{rms,max}/U_e$ value goes beyond 0.1 at the point of separation.

On the whole, we find that the streaky structures are not general flow features for all the separated flows at an enhanced level of FST. The dominant KH instability mechanism is not bypassed for both the geometry- and pressure-induced separation bubbles under the free-stream turbulent intensity up to 3.3 %, even though the streaky structures are present for the PISB.

Declaration of interests. The authors report no conflict of interest.

Author ORCIDs.

S. Mohamed Aniffa https://orcid.org/0000-0001-9633-0976;

A.C. Mandal https://orcid.org/0000-0002-4933-4461.

Appendix A. Statistical flow characteristics in the spanwise plane

The linear stochastic analysis has been carried out to consolidate the instantaneous observations shown in figure 20. Using this statistical analysis, one can estimate the conditional average of a process with unconditional data (Christensen & Adrian 2001; Adrian 2007). The conditional average of the fluctuating velocity field (u, w) for a given u velocity event in the spanwise plane (Tomkins & Adrian 2003; Mandal & Dey 2011) can be expressed as

$$\langle u_j(x')|u(x)\rangle \approx \frac{\langle u(x)u_j(x')\rangle}{\langle u(x)u(x)\rangle}u(x), \tag{A1}$$

where u_j indicates u and w for $j = 1$ and 2, respectively, in the present study. The (A1) indicates that a conditional average can approximately be estimated by the unconditional two-point correlation. Further details of this analysis are available in Adrian (2007).

Figure 25(a–d) shows the conditional structures for the cases displayed in figure 20 for a given negative u velocity. One may note in figure 25(a,b) that there are two counter-rotating vortices with a negative u fluctuation in between these two vortices, indicating the presence of Λ-type structures (Mandal & Dey 2011). The signature of these Λ-type structures in the separated shear layer indicates the three dimensionality of the shear layer for both the GISB-N2 and GISN-B2 cases at $Re = 1529$. On the other hand, the conditional structure in figure 25(c) for the PISB-N2 case shows the signature of a 2-D shear layer, whereas the
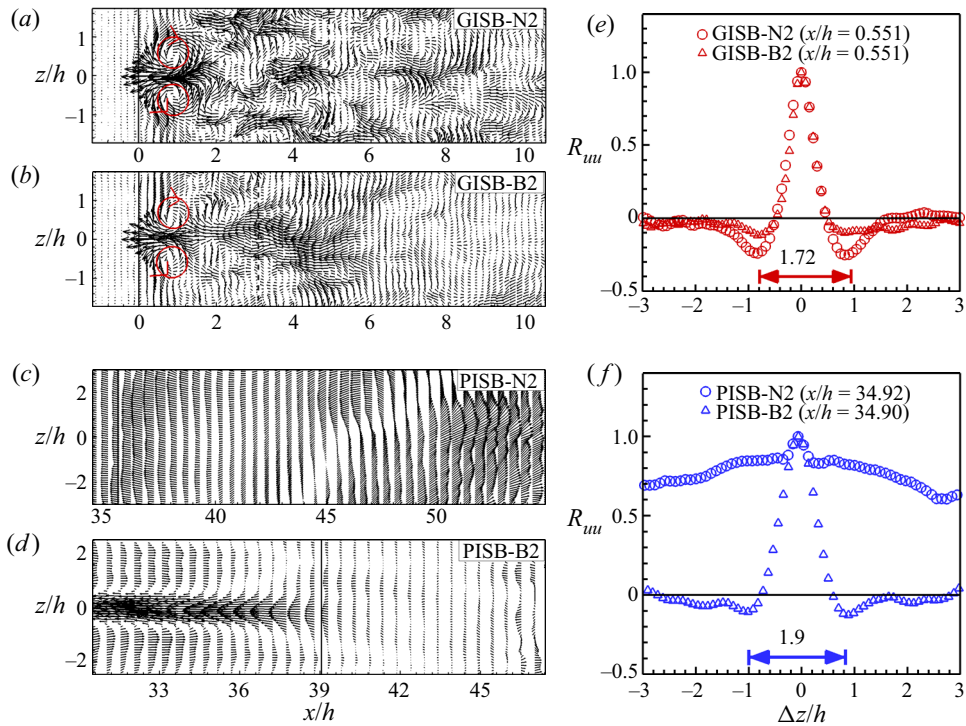
Figure 25. A linear stochastic estimate of the fluctuating velocity components (u and w) in the spanwise plane. Results are shown for the (*a*) GISB-N2 case, (*b*) GISB-B2 case, (*c*) PISB-N2 case, (*d*) PSIB-B2 case. Plots (*e*) and (*f*) represent R_{uu} in the spanwise direction for the GISB and PISB cases, respectively.

conditional structure in figure 25(*d*) for the PISB-B2 case clearly shows the presence of low- and high-velocity streaks, i.e. the presence of the K mode.

The spatial correlation of the fluctuating streamwise velocity in the spanwise direction is defined as

$$R_{uu} = \frac{\overline{u(x_r, z_r)u(x_r, z_r + \Delta z)}}{\sqrt{\overline{u^2(x_r, z_r)}}\sqrt{\overline{u^2(x_r, z_r + \Delta z)}}}, \tag{A2}$$

where (x_r, z_r) and Δz indicate the reference location and the spatial separation in the spanwise direction, as shown in figures 25(*e*) and 25(*f*), for the corresponding GISB and PISB cases, respectively. The spanwise length scales of the separated shear layer, estimated as the distance between the peak negative values of the correlation coefficients (see figure 25*e*), are found to be approximately the same (i.e. 1.72) for both the GISB cases without and with an enhanced level of FST. High values of the correlation coefficient in the spanwise direction, as shown in figure 25(*f*), for the PISN-N2 case indicate the presence of nearly a 2-D shear layer. Whereas the correlation coefficient, as shown in figure 25(*f*), for the PISN-B2 case show that the average streak spacing (i.e. 1.9) in the spanwise direction (Mandal *et al.* 2010) are comparable with the spanwise wavelength of the 3-D shear layer found in the GISB cases. In the recent study by Dellacasagrande *et al.* (2021), it has been reported that the half-streak spacing (Δz_{min}) value converges to 3 and 5, if it is normalized by the values of displacement and momentum thickness that correspond to the turbulent region, respectively. The $\Delta z_{min}/\delta_r^*$ and $\Delta z_{min}/\theta_r$ values for

957 A19-38

the cases GISB-N2, GISB-B2 and PISB-B2 are found to vary from 1.3–1.6 and 5–6.8, respectively, where δ_r^* and θ_r are the displacement and momentum thickness value at the point of reattachment. It shows that only $\Delta z_{min}/\theta_r$ are comparable with Dellacasagrande *et al.* (2021) but not $\Delta z_{min}/\delta_r^*$. One may note that the roller/vortex structures are not found in the instantaneous PIV realizations, as shown in figure 20. This is due to the fact that the vortex shedding plane lies above the measurement plane. The above figures only show the conditional structures near the separation point.

REFERENCES

ADRIAN, R.J. 2007 Conditional averages and stochastic estimation. In *Handbook of Experimental Fluid Mechanics* (ed. A.L. Yarin C. Tropea & J.F. Foss), pp. 1370–1378. Springer.

ADRIAN, R.J., CHRISTENSEN, K.T. & LIU, Z.C. 2000 Analysis and interpretation of instantaneous turbulent velocity fields. *Exp. Fluids* **29**, 275–290.

ALKISLAR, M.B., KROTHAPALLI, A. & LOURENCO, L.M. 2003 Structure of a screeching rectangular jet: a stereoscopic particle image velocimetry study. *J. Fluid Mech.* **489**, 121–154.

ANIFFA, S.M. 2023 An experimental study on the characteristics of separated flows at an elevated level of freestream turbulence (under preparation). PhD thesis, Indian Institute of Technology Kanpur, India.

AVANCI, M.P., RODRÍGUEZ, D. & ALVES, L.S.D.B. 2019 A geometrical criterion for absolute instability in separated boundary layers. *Phys. Fluids* **31** (1), 014103.

BALAMURUGAN, G. & MANDAL, A.C. 2017 Experiments on localized secondary instability in bypass boundary layer transition. *J. Fluid Mech.* **817**, 217–263.

BALAMURUGAN, G., RODDA, A., PHILIP, J. & MANDAL, A.C. 2020 Characteristics of the turbulent non-turbulent interface in a spatially evolving turbulent mixing layer. *J. Fluid Mech.* **894**, A4.

BALTZER, J.R. & ADRIAN, R.J. 2011 Structure, scaling, and synthesis of proper orthogonal decomposition modes of inhomogeneous turbulence. *Phys. Fluids* **23**, 015107.

BALZER, W. & FASEL, H.F. 2016 Numerical investigation of the role of free-stream turbulence in boundary-layer separation. *J. Fluid Mech.* **801**, 289–321.

BERKOOZ, G., HOLMES, P. & LUMLEY, J.L. 1993 The proper orthogonal decomposition in the analysis of turbulent flows. *Annu. Rev. Fluid Mech.* **25**, 539–575.

BOUTILIER, M.S.H. & YARUSEVYCH, S. 2010 Inviscid spatial linear stability analysis of separated shear layers based on experimental data. In *40th Fluid Dynamics Conference and Exhibit, Chicago, IL, USA*, AIAA 2010-4293. AIAA.

BOUTILIER, M.S.H. & YARUSEVYCH, S. 2012 Separated shear layer transition over an airfoil at a low Reynolds number. *Phys. Fluids* **24** (8), 084105.

BRUN, C., AUBRUN, S., GOOSSENS, T. & RAVIER, P. 2008 Coherent structures and their frequency signature in the separated shear layer on the sides of a square cylinder. *Flow Turbul. Combust.* **81** (1–2), 97–114.

CASTRO, I.P. & HAQUE, A. 1988 The structure of a shear layer bounding a separation region. Part 2. Effects of free-stream turbulence. *J. Fluid Mech.* **192**, 577–595.

CHAURASIA, H.K. & THOMPSON, M.C. 2011 Three-dimensional instabilities in the boundary-layer flow over a long rectangular plate. *J. Fluid Mech.* **681**, 411–433.

CHERRY, N.J., HILLIER, R. & LATOUR, M.E.M.P. 1984 Unsteady measurements in a separated and reattaching flow. *J. Fluid Mech.* **144**, 13–46.

CHONG, M.S., PERRY, A.E. & CANTWELL, B.J. 1990 A general classification of three-dimensional flow fields. *Phys. Fluids* **2**, 765–777.

CHRISTENSEN, K.T. & ADRIAN, R.J. 2001 Statistical evidence of hairpin vortex packets in wall turbulence. *J. Fluid Mech.* **431**, 433–443.

COLEMAN, H.W. & STEELE, W.G. 2018 *Experimentation, Validation, and Uncertainty Analysis for Engineers*. John Wiley & Sons.

COULL, J.D. & HODSON, H.P. 2011 Unsteady boundary-layer transition in low-pressure turbines. *J. Fluid Mech.* **681**, 370–410.

DABARIA, V. 2015 Linear stability analysis of measured inflectional velocity profiles in separated boundary layer flows. Master's thesis, Indian Institute of Technology, Kanpur, India.

DELLACASAGRANDE, M., BARSI, D., LENGANI, D., SIMONI, D. & VERDOYA, J. 2020 Response of a flat plate laminar separation bubble to Reynolds number, free-stream turbulence and adverse pressure gradient variation. *Exp. Fluids* **61** (6), 1–17.

DELLACASAGRANDE, M., LENGANI, D., SIMONI, D., PRALITS, J.O., DUROVICH, K., HANIFI, A. & HENNINGSON, D. 2021 Statistical characterization of free-stream turbulence induced transition under variable Reynolds number, free-stream turbulence, and pressure gradient. *Phys. Fluids* **33** (9), 094115.

DHIMAN, A. 2015 Experimental investigations of the effects of increased free-stream turbulence levels on a pressure induced separation bubble. Master's thesis, Indian Institute of Technology, Kanpur, India.

DIWAN, S.S., CHETAN, S.J. & RAMESH, O.N. 2006 On the bursting criterion for laminar separation bubbles. In *Sixth IUTAM Symposium on Laminar–Turbulent Transition* (ed. R. Govindarajan), pp. 401–407. Springer.

DIWAN, S.S. & RAMESH, O.N. 2009 On the origin of the inflectional instability of a laminar separation bubble. *J. Fluid Mech.* **629**, 263–298.

DIWAN, S.S. & RAMESH, O.N. 2012 Relevance of local parallel theory to the linear stability of laminar separation bubbles. *J. Fluid Mech.* **698**, 468–478.

DOVGAL, A.V., KOZLOV, V.V. & MICHALKE, A. 1994 Laminar boundary layer separation: instability and associated phenomena. *Prog. Aerosp. Sci.* **30** (1), 61–94.

FITZGERALD, E.J. & MUELLER, T.J. 1990 Measurements in a separation bubble on a airfoil using laser velocimetry. *AIAA J.* **28** (4), 584–592.

FRANSSON, J.H.M., MATSUBARA, M. & ALFREDSSON, P.H. 2005 Transition induced by freestream turbulence. *J. Fluid Mech.* **527**, 1–25.

GASTER, M. 1967 The structure and behaviour of separation bubbles. *Aeronautical Research Council Reports and Memoranda* No. 3595. Aeronautical Research Council.

GUI, L. & WERELEY, S.T. 2002 A correlation-based continuous window-shift technique to reduce the peak-locking effect in digital PIV image evaluation. *Exp. Fluids* **32** (4), 506–517.

HÄGGMARK, C. 2000 Investigations of disturbances developing in a laminar separation bubble flow. *Tech. Rep.* Royal Institute of Technology, Department of Mechanics, Stockholm, Sweden.

HÄGGMARK, C.P., BAKCHINOV, A.A. & ALFREDSSON, P.H. 2000 Experiments on a two-dimensional laminar separation bubble. *Phil. Trans. R. Soc. Lond.* A **358** (1777), 3193–3205.

HALFON, E., NISHRI, B., SEIFERT, A. & WYGNANSKI, I. 2004 Effects of elevated free-stream turbulence on actively controlled separation bubble. *Trans. ASME J. Fluids Engng* **126** (6), 1015–1024.

HANSON, R.E., BUCKLEY, H.P. & LAVOIE, P. 2012 Aerodynamic optimization of the flat-plate leading edge for experimental studies of laminar and transitional boundary layers. *Exp. Fluids* **53**, 863–871.

HASAN, N. & SANGHI, S. 2007 Proper orthogonal decomposition and low-dimensional modelling of thermally driven two-dimensional flow in a horizontal rotating cylinder. *J. Fluid Mech.* **573**, 265–295.

HILLIER, R. & CHERRY, N.J. 1981 The effects of stream turbulence on separation bubbles. *J. Wind Engng Ind. Aerodyn.* **8** (1), 49–58.

HOLMAN, J.P. 2012 *Experimental methods for engineers*, vol. s1-VIII, 8th edn. McGraw Hill.

HOSSEINVERDI, S. & FASEL, H.F. 2019 Numerical investigation of laminar–turbulent transition in laminar separation bubbles: the effect of free-stream turbulence. *J. Fluid Mech.* **858**, 714–759.

ISTVAN, M.S. & YARUSEVYCH, S. 2018 Effects of free-stream turbulence intensity on transition in a laminar separation bubble formed over an airfoil. *Exp. Fluids* **59** (3), 52.

JACOBS, R.G. & DURBIN, P.A. 2001 Simulations of bypass transition. *J. Fluid Mech.* **428**, 185–212.

KARP, M. & HACK, M.J.P. 2020 Optimal suppression of a separation bubble in a laminar boundary layer. *J. Fluid Mech.* **892**, A23.

KIRK, T.M. & YARUSEVYCH, S. 2017 Vortex shedding within laminar separation bubbles forming over an airfoil. *Exp. Fluids* **58** (5), 43.

KIYA, M. & SASAKI, K. 1983a Free-stream turbulence effects on a separation bubble. *J. Wind Engng Ind. Aerodyn.* **14** (1), 375–386.

KIYA, M. & SASAKI, K. 1983b Structure of a turbulent separation bubble. *J. Fluid Mech.* **137**, 83–113.

KRUSE, N., GUNTHER, A. & ROHR, P.R.V. 2003 Dynamics of large-scale structures in turbulent flow over wavy wall. *J. Fluid Mech.* **485**, 87–96.

LANE, J.C. & LOEHRKE, R.I. 1980 Leading edge separation from a blunt plate at low Reynolds number. *Trans. ASME J. Fluids Engng* **102** (4), 494–496.

LANG, M., RIST, U. & WAGNER, S. 2004 Investigations on controlled transition development in a laminar separation bubble by means of LDA and PIV. *Exp. Fluids* **36** (1), 43–52.

LANGARI, M. & YANG, Z. 2013 Numerical study of the primary instability in a separated boundary layer transition under elevated free-stream turbulence. *Phys. Fluids* **25** (7), 074106.

LENGANI, D., SIMONI, D., UBALDI, M. & ZUNINO, P. 2014 POD analysis of the unsteady behavior of a laminar separation bubble. *Expl Therm. Fluid Sci.* **58**, 70–79.

LENGANI, D., SIMONI, D., UBALDI, M., ZUNINO, P. & BERTINI, F. 2017 Experimental study of free-stream turbulence induced transition in an adverse pressure gradient. *Expl Therm. Fluid Sci.* **84**, 18–27.

LI, Y. & GASTER, M. 2006 Active control of boundary-layer instabilities. *J. Fluid Mech.* **550**, 185–205.

LI, H.J. & YANG, Z. 2019 Separated boundary layer transition under pressure gradient in the presence of free-stream turbulence. *Phys. Fluids* **31** (10), 104106.

LOURENCO, L.M. & KROTHAPALLI, A. 2000 TRUE resolution PIV: a mesh-free second order accurate algorithm. In *Proceedings of the International Conference in Applications of Lasers to Fluid Mechanics, Lisbon, Portugal*.

MANDAL, A.C. & DEY, J. 2011 An experimental study of boundary layer transition induced by a cylinder wake. *J. Fluid Mech.* **684**, 60–84.

MANDAL, A.C., VENKATAKRISHNAN, L. & DEY, J. 2010 A study on boundary-layer transition induced by free-stream turbulence. *J. Fluid Mech.* **660**, 114–146.

MARXEN, O., LANG, M. & RIST, U. 2012 Discrete linear local eigenmodes in a separating laminar boundary layer. *J. Fluid Mech.* **711**, 1–26.

MARXEN, O., LANG, M. & RIST, U. 2013 Vortex formation and vortex breakup in a laminar separation bubble. *J. Fluid Mech.* **728**, 58–90.

MARXEN, O., LANG, M., RIST, U., LEVIN, O. & HENNINGSON, D.A.N.S. 2009 Mechanisms for spatial steady three-dimensional disturbance growth in a non-parallel and separating boundary layer. *J. Fluid Mech.* **634**, 165–189.

MARXEN, O., LANG, M., RIST, U. & WAGNER, S. 2003 A combined experimental/numerical study of unsteady phenomena in a laminar separation bubble. *Flow Turbul. Combust.* **71** (1–4), 133–146.

MATSUBARA, M. & ALFREDSSON, P.H. 2001 Disturbance growth in boundary layers subjected to free-stream turbulence. *J. Fluid Mech.* **430**, 149–169.

MCAULIFFE, B.R. & YARAS, M.I. 2010 Transition mechanisms in separation bubbles under low-and elevated-freestream turbulence. *Trans. ASME J. Turbomach.* **132** (1), 011004.

MEYER, K.E., PEDERSEN, J.M. & ÖZCAN, O. 2007 A turbulent jet in crossflow analysed with proper orthogonal decomposition. *J. Fluid Mech.* **583**, 199–227.

MICHELIS, T., KOTSONIS, M. & YARUSEVYCH, S. 2018*a* Spanwise flow development within a laminar separation bubble under natural and forced transition. *Expl Therm. Fluid Sci.* **96**, 169–179.

MICHELIS, T., YARUSEVYCH, S. & KOTSONIS, M. 2018*b* On the origin of spanwise vortex deformations in laminar separation bubbles. *J. Fluid Mech.* **841**, 81–108.

MONKEWITZ, P.A. & HUERRE, P. 1982 Influence of the velocity ratio on the spatial instability of mixing layers. *Phys. Fluids* **25** (7), 1137–1143.

OTA, T., ASANO, Y. & OKAWA, J.-I. 1981 Reattachment length and transition of the separated flow over blunt flat plates. *Bull. JSME* **24** (192), 941–947.

PAULEY, L.L. 1994 Structure of local pressure-driven three-dimensional transient boundary-layer separation. *AIAA J.* **32** (5), 997–1005.

PAULEY, L.L., MOIN, P. & REYNOLDS, W.C. 1990 The structure of two-dimensional separation. *J. Fluid Mech.* **220**, 397–411.

PIERREHUMBERT, R.T. & WIDNALL, S.E. 1982 The two-and three-dimensional instabilities of a spatially periodic shear layer. *J. Fluid Mech.* **114**, 59–82.

RAFFEL, M., WILLERT, C.E., SCARANO, F., KÄHLER, C.J., WERELEY, S.T. & KOMPENHANS, J. 2018 *Particle Image Velocimetry: A Practical Guide*. Springer.

ROBINET, J.C. 2013 Instabilities in laminar separation bubbles. *J. Fluid Mech.* **732**, 1–4.

RODRÍGUEZ, D., GENNARO, E.M. & SOUZA, L.F. 2021 Self-excited primary and secondary instability of laminar separation bubbles. *J. Fluid Mech.* **906**, A13.

SASAKI, K. & KIYA, M. 1991 Three-dimensional vortex structure in a leading-edge separation bubble at moderate Reynolds numbers. *Trans. ASME J. Fluids Engng* **113** (3), 405–410.

SCHMID, P.J. & HENNINGSON, D.S. 2001 *Stability and Transition in Shear Flows*. Springer.

SIMONI, D., LENGANI, D., UBALDI, M., ZUNINO, P. & DELLACASAGRANDE, M. 2017 Inspection of the dynamic properties of laminar separation bubbles: free-stream turbulence intensity effects for different Reynolds numbers. *Exp. Fluids* **58** (6), 66.

SIMONI, D., UBALDI, M., ZUNINO, P. & BERTINI, F. 2012*a* Transition mechanisms in laminar separation bubbles with and without incoming wakes and synthetic jet effects. *Exp. Fluids* **53** (1), 173–186.

SIMONI, D., UBALDI, M., ZUNINO, P., LENGANI, D. & BERTINI, F. 2012*b* An experimental investigation of the separated-flow transition under high-lift turbine blade pressure gradients. *Flow Turbul. Combust.* **88** (1–2), 45–62.

SIROVICH, L. 1987 Turbulence and the dynamics of coherent structures. Part 1. Coherent structures. *Q. Appl. Maths* **45**, 561–571.

SPALART, P.R. & STRELETS, M.K. 2000 Mechanisms of transition and heat transfer in a separation bubble. *J. Fluid Mech.* **403**, 329–349.

STEVENSON, J.P.J., NOLAN, K.P. & WALSH, E.J. 2016 Particle image velocimetry measurements of induced separation at the leading edge of a plate. *J. Fluid Mech.* **804**, 278–297.

TAFTI, D.K. & VANKA, S.P. 1991 A three-dimensional numerical study of flow separation and reattachment on a blunt plate. *Phys. Fluids* A **3** (12), 2887–2909.

TANI, I. 1964 Low-speed flows involving bubble separations. *Prog. Aerosp. Sci.* **5**, 70–103.

THIELICKE, W. 2014 The flapping flight of birds. PhD thesis, University of Groningen.

THOMPSON, M.C. 2012 Effective transition of steady flow over a square leading-edge plate. *J. Fluid Mech.* **698**, 335–357.

TOMKINS, C.D. & ADRIAN, R.J. 2003 Spanwise structure and scale growth in turbulent boundary layers. *J. Fluid Mech.* **490**, 37–74.

VILLERMAUX, E. 1998 On the role of viscosity in shear instabilities. *Phys. Fluids* **10** (2), 368–373.

VOLINO, R.J. 2002 Separated flow transition under simulated low-pressure turbine airfoil conditions. Part 2. Turbulence spectra. *Trans. ASME J. Turbomach.* **124** (4), 656–664.

WATMUFF, J.H. 1997 Detrimental effects of almost immeasurably small free-stream nonuniformities generated by wind tunnel screens. In *35th Aerospace Sciences Meeting and Exhibit, Reno, NV, USA*, AIAA 97-0228. AIAA.

WATMUFF, J.H. 1999 Evolution of a wave packet into vortex loops in a laminar separation bubble. *J. Fluid Mech.* **397**, 119–169.

WESTIN, K.J.A., BOIKO, A.V., KLINGMANN, B.G.G., KOZLOV, V.V. & ALFREDSSON, P.H. 1994 Experiments in a boundary layer subjected to free stream turbulence. Part 1. Boundary layer structure and receptivity. *J. Fluid Mech.* **281**, 193–218.

WHITE, F.M. 2006 *Viscous Fluid Flow*. McGraw Hill.

XU, D. & WU, X. 2021 Elevated low-frequency free-stream vortical disturbances eliminate boundary-layer separation. *J. Fluid Mech.* **920**, A14.

YANG, Z. 2019 On bypass transition in separation bubbles: a review. *Propul. Power Res.* **8** (1), 23–34.

YANG, Z. & ABDALLA, I.E. 2005 Effects of free-stream turbulence on large-scale coherent structures of separated boundary layer transition. *Intl J. Numer. Meth. Fluids* **49** (3), 331–348.

YANG, Z. & ABDALLA, I.E. 2009 Effects of free-stream turbulence on a transitional separated–reattached flow over a flat plate with a sharp leading edge. *Intl J. Heat Fluid Flow* **30** (5), 1026–1035.

YANG, Z. & VOKE, P.R. 2001 Large-eddy simulation of boundary-layer separation and transition at a change of surface curvature. *J. Fluid Mech.* **439**, 305–333.

YAVUZKURT, S. 1984 A guide to uncertainty analysis of hot-wire data. *Trans. ASME I: J. Fluids Engng* **106**, 181–186.